8. Natural Time Analysis of Dynamical Models

Abstract. We apply here the natural time analysis to the time series of the avalanches in several SOC models as well as to other dynamical models. First, in a simple deterministic SOC system introduced to describe avalanches in stick–slip phenomena that belongs to the same universality class as the "train" model for earthquakes introduced by Burridge and Knopoff, we find that the value $\kappa_1 = 0.070$ can be considered as quantifying the extent of the organization of the system at the onset of the critical stage. Second, in the conservative case of the Olami–Feder–Christensen (OFC) earthquake model, the value $\kappa_1 = 0.070$ is accompanied by an abrupt exponential increase of the avalanche size which is indicative of the approach to a critical behavior. In the non-conservative case of OFC, in the later part of the transient period, coherent domains of the strain field gradually develop accompanied by κ_1 values close to 0.070. Furthermore, there is a non-zero change ΔS of the entropy in natural time under time reversal, thus reflecting predictability in the OFC model. Third, an explanation for the validity of the condition $\kappa_1 = 0.070$ for critical systems on the basis of the dynamic scaling hypothesis is forwarded. Fourth, when quenching the 2D Ising model at temperatures close to but below T_c, which is qualitatively similar with the pressure stimulated currents SES generation model, and set $Q_k = |M_k|$ (where M_k stands for the evolution of the magnetization per spin), we find $\kappa_1 = 0.070$. Fifth, in a deterministic version of the original Bak–Tang–Wiesenfeld sandpile model, the value $\kappa_1 \approx 0.070$ is reached during the transient to the self-organized criticality. Finally, natural time analysis of the avalanches observed in laboratory experiments on three-dimensional ricepiles and on the penetration of the magnetic flux into thin films of high T_c superconductors, leads to κ_1 values around $\kappa_1 = 0.070$. A further investigation of the experiment on ricepiles reveals that the *sequential order* of the avalanches captured by the natural time analysis is of profound importance for establishing the SOC state and constitutes the basis for the observation of the result $\kappa_1 \approx 0.070$.

P.A. Varotsos et al., *Natural Time Analysis: The New View of Time: Precursory Seismic Electric Signals, Earthquakes and other Complex Time Series*, Springer Praxis Books, DOI 10.1007/978-3-642-16449-1_8,

8.1 Is self-organized criticality (SOC) compatible with prediction? Recent aspects. The models analyzed here in natural time

The SOC concept, that has been originally introduced by Bak, Tang and Wiesenfeld [6] using as an example the sandpile model, was an attempt to explain the ubiquity of scale invariance in nature (see also Refs. [44, 74]). Systems, in general, are termed self-organized critical if they reach a stationary state (after a transient during which the system acquires criticality [32, 33]) characterized by power laws without the need for fine-tuning an external parameter, for example the temperature or pressure. There is more or less a general tendency [85] on confining the term self-organized critical to those systems that are slowly driven and that display fast, avalanche-like dissipation events. In other words, in SOC systems, the competition between a driving force that very slowly injects energy and the dynamics of local thresholds can drive the system into a *critical state* where a minor perturbation can trigger an avalanche of any size and duration [6, 7, 66]. In particular, in the original sandpile model, the random, slow addition of "blocks" in a two-dimensional lattice (along with a local conservation law) drives the system into a critical state, where power law distributed avalanches maintain a steady regime far from equilibrium.

The fact that avalanches were taken [6] as uncorrelated in the original SOC sandpile model, has been used as an argument that is not possible to predict the occurrence of large avalanches (relevant claims are cited in Refs. [66, 65]). A belief has been expressed that power law distributed avalanches are inherently unpredictable, which came from the concept of SOC, but interpreted in the way that, at any moment, any small avalanche can eventually cascade to a large event.

However, prediction is possible, because the system is not *at*, but *close to*, the critical state [21, 66].

This, became clear from the accumulated theoretical and experimental evidence, which could be summarized as follows (see also § 6.5.3). First, some cellular automaton SOC models have been analyzed for the predictability of very large avalanches (responsible for the cut-off on the power law distribution) [62] and in addition precursors of large events have been identified [41, 67] in dissipative or hierarchical lattices. Second, the prediction of extreme avalanches in self-organized critical sandpiles have been studied in recent detailed numerical studies [32] which showed that: (a) particularly large events in a close to SOC system can be predicted on the basis of past observations; (b) the predictive power stems from temporal correlations which are pure finite size effects, i.e., it disappears in the infinite system size limit as all avalanches become independent of each other; (c) under variation of the system size, predictability persists if the magnitude used to define extreme events is scaled linearly in the maximal possible avalanche size. It was also clarified [33] that SOC seems to be an unsuitable mechanism for the explanation of the extreme events that occur in clusters. Third, experimental work has recently demonstrated [66] the possibility of avalanche prediction in the classical SOC paradigm, i.e., a pile of grains: by knowing the position of every grain in a two-dimensional pile, avalanches of moving grains do follow a distinct power law distribution, but large avalanches are found [66] to

Table 8.1 Compilation of the 14 cases described in this monograph in which the condition $\kappa_1 = 0.070$ has been ascertained.

No.	Case	Class
1	SES activities (Section 4.2)	Field experiments
2	Seismicity preceding major EQs (Sections 7.1 to 7.5)	"
3	Ricepiles (§ 8.5.1)	Laboratory measurements
4	Magnetic flux avalanches in high T_c superconductors (§ 8.5.2)	"
5	Burridge & Knopoff "train" EQ model (§ 8.2.2)	Dynamical models
6	Olami–Feder–Christensen EQ model (conservative case, § 8.3.2) and "foreshocks" in the non-conservative case (§ 8.3.3)	"
7	Dynamic scaling hypothesis with $z = 2.0$–2.4 (Section 8.4, § 8.4.3)	"
8	Deterministic version of the original sandpile SOC model (§ 8.4.2)	"
9	Generalized stochastic directed SOC model (§ 8.5.2)	"
10	2D Ising model quenched close to, but below, T_c (§ 8.4.1)	Other models
11	Pressure stimulated currents model for SES generation (§ 2.4.2)	"
12	fBm time series with DFA exponent $\alpha = 1$ (§ 3.4.3)	"
13	Stochastic Cantor set: p-model describing turbulence (§ 6.2.5)	"
14	Power law distributed uncorrelated energy bursts with $\gamma = 1.87$ (§ 2.5.4, Fig. 2.6)	"

be preceded on the average by continuous detectable variations in the internal structure of the pile.

To answer the aforementioned question on predictability, in this Chapter we will analyze in natural time the time series of avalanches in some dynamical models including typical SOC examples like sandpiles, as well as in laboratory measurements on ricepiles and magnetic flux penetration in high T_c superconductors which are believed to be SOC systems.

Table 8.1 includes all 14 cases discussed in this monograph where the condition $\kappa_1 \approx 0.070$ has been ascertained, thus strengthening the conjecture that: *if* a system acquires criticality, the condition $\kappa_1 = 0.070$ holds (but *not* the inverse as for example case No. 14).

8.2 Natural time analysis of the Burridge & Knopoff "train" earthquake model

8.2.1 The earthquake model proposed by Burridge & Knopoff. The "train" model. Introduction

An earthquake is a stick–slip dynamical instability of a pre-existing fault driven by the motion of a tectonic plate [71, 72]. A relatively simple dynamical model that contains much of the essential physics of earthquake faults is the so-called spring-block model originally proposed [14] by Burridge and Knopoff (BK). It consists of an assembly of blocks, each of which is connected via elastic springs to the nearest neighboring blocks.

The blocks are also connected to the driving plate by elastic springs and rest on a surface with a velocity-weakening stick–slip friction force (note that the friction force decreases as the velocity is increased). When the force acting on a block overcomes the static friction with the surface, the block slips. Then a redistribution of forces takes place in the neighbors that eventually trigger new displacements. An EQ event is defined as a cluster of blocks that move (slip) due to the initial slip of a single block. A numerical study in one dimension had already been made by BK, and later Carlson, Langer and others [18, 19] proceeded to more extensive studies of the one-dimensional and two-dimensional BK models focusing on the magnitude distribution of EQ events. Spatiotemporal correlations of the 2D BK model have been studied [55] by considering also long-range inter-block interactions.

In the BK model studied by Carlson, Langer and others, each block is connected, as mentioned above, to the driving element. To model the dynamics of EQs, Burridge and Knopoff in their original work [14] also studied the case of a chain of blocks (situated on a rough surface with friction) connected by elastic springs and pulled only at one end with a constant small velocity. The dynamics of the model is as follows. All the blocks are initially at rest. As the driver pulls the first block, the latter remains stuck until the elastic force overcomes the static friction. When this occurs, the first block will move a little. Such small events (or EQs) will continue and increase the elastic force on the second block. When the elastic force on the second block overcomes the friction force, an event involving the two blocks will occur. The dynamics continues with events involving three, four, five or all the blocks in the system. This model is usually called the "train" model since it has some similarity with a train, where the driving force is applied only at one end of the chain (e.g., Ref. [75]). The dynamics here is governed by coupled ordinary differential equations which makes its study very time-consuming. To make this system more amenable to computer simulations, de Sousa Vieira [76] introduced a continuous cellular automaton that exhibits SOC and belongs to the same universality class as the "train" model. This *deterministic* one-dimensional model, for the avalanches in stick–slip phenomena, which is very close to the case of an array of connected pendulums first discussed by Bak et al. [6], is defined as follows (see Refs. [76, 26, 70]). Consider a one-dimensional system, where a continuous (force) variable $f_l \geq 0$ is associated with each site l, $l = 1, 2, \ldots, L$. Initially all f_l have the same value f_0 which lies below a threshold f_{th}. One can set $f_{th} = 1.0$ without loss of generality. The basic time step consists of varying the force on the first site according to $f_1 = f_{th} + \delta f$; the system then relaxes with a conservative redistribution of the forces at the site $f_l \geq f_{th}$ (toppling site) and its nearest neighbors according to $f_l = \Psi(f_l - f_{th})$ and $f_{l\pm1} = f_{l\pm1} + \Delta f/2$, where Δf is the change of force at the overcritical site and $\Psi(x)$ a periodic nonlinear function. This condition mimics the redistribution of forces when the block l is displaced (stick–slips) by Δx_l during an 'earthquake' in the "train" model [76]. The relaxation continues until all sites have $f_l < f_{th}$ for all l. The size of the 'earthquake' corresponds to the number of topplings, s, required for the system to relax, and is considered here as the appropriate value of Q_k in natural time. Then, the driving force at the first site sets in again. This is complemented by open boundary conditions; i.e., the force is 'lost' at $l = 1$ and $l = L$. The nonlinear periodic function used here (which means that, when considering that the force supposed mimics the net effect of the two forces in the "train" model, i.e., the elastic and the friction forces, the periodicity of the elastic force dominates over the form of the friction force) is similar to

the one used in Refs. [76, 26], i.e., a sawtooth function $\Psi(x) = 1 - ax + [ax]$, where $[\ldots]$ denotes the integer part of ax and a is a number. It was shown [76] that such a system evolves to a SOC state where the avalanche distributions are scale-free, limited only by the overall system size.

8.2.2 Natural time analysis of the "train" model

In Fig. 8.1, we present the results obtained from the deterministic one-dimensional SOC system described above in § 8.2.1 that belongs, as mentioned, to the same universality class as the "train" model for EQs. The same parameters as in Ref. [26], i.e., $L = 1024$, $a = 4$, $f_0 = 0.87$ and $\delta f = 0.1$, have been used. In Fig. 8.1(a), the number of topplings s is plotted in red versus the avalanche number i for the first 160,000 avalanches which shows in fact how these series of avalanches can be read in natural time. The blue curve in Fig. 8.1(a), shows how the quantity κ_1 evolves avalanche by avalanche. There, we also plot in green the total force $X(i)$ of the system after each avalanche, computed from $X(i) = \sum_{l=1}^{L} f_l(i)$, whose stabilization provides [26] a measure of the approach to SOC. An inspection of Fig. 8.1(a) reveals that (after the transient and hence) when the system enters into the

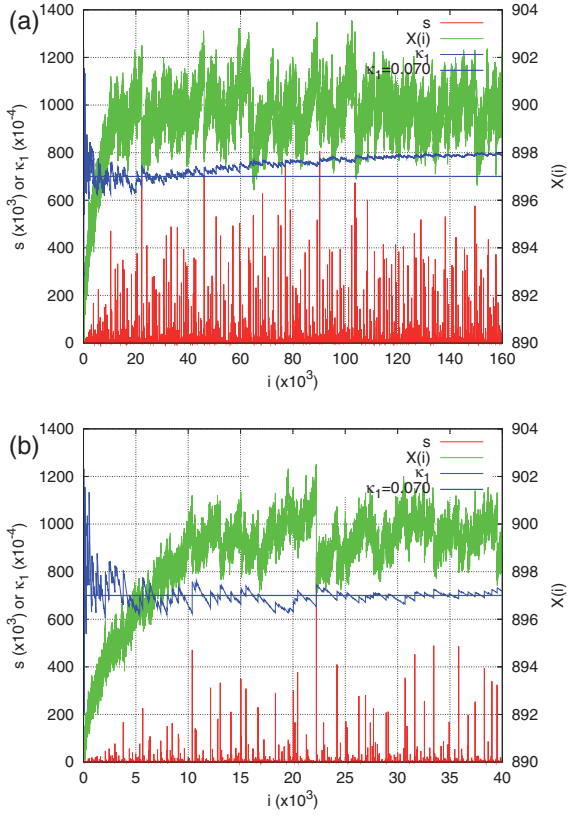

Fig. 8.1 The results of the model discussed in the text for 160,000 (a) and 40,000 (b) avalanches as read in natural time, for $L = 1024$, $a = 4$, $f_0 = 0.87$ and $\delta f = 0.1$. The avalanche size s is depicted by red color, and the variance κ_1 by blue color. The thick blue line corresponds to $\kappa_1 = 0.070$. The total force of the system after each avalanche $X(i)$ is plotted with green color and read in the right scale. For an extension of this figure to 10^6 avalanches see Fig. 8.2. Taken from Ref. [82].

critical state, the κ_1 value fluctuates around 0.070 (designated by the thick blue line). The latter becomes clear in Fig. 8.1(b), which reproduces Fig. 8.1(a) but in an enlarged time scale for the first 40,000 avalanches and shows that for $i > 5,000$ (i.e., just when the system enters into the SOC state) κ_1 scatters around 0.070. This behavior has been verified for a wide range of parameters L, a, f_0 and δf just before the SOC state is reached. Note that, once the statistically steady SOC state is established, the κ_1 value gradually increases reaching the corresponding value of $\kappa_u = 1/12$ of a "uniform" distribution (see § 2.1.3). This can be seen in Fig. 8.2 which has been plotted for 10^6 avalanches. The model discussed here leads to a power law with a realistic b value of the Gutenberg–Richter law. In particular, de Sousa Vieira [76] concluded that the distribution of avalanche sizes s is a power law with an exponent $\tau \approx 1.54$ that corresponds to $b \approx 0.81$. This lies in the range (0.8 to 1.2) of the b values found experimentally (see Section 6.1). In spite of this agreement, however, we note that the BK model cannot account for the observed spatiotemporal complexity of seismicity, e.g. the Omori law for aftershocks [55].

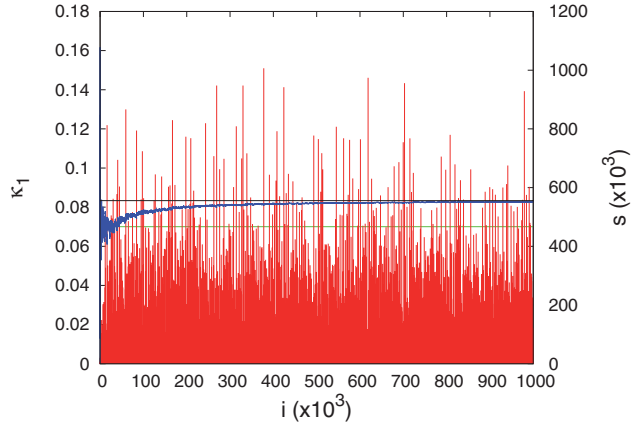

Fig. 8.2 The results of the model discussed in the text for 10^6 avalanches. The parameters (as well as the symbols) here are the same as in Fig. 8.1 (except that the total force $X(i)$ is not plotted, for the sake of simplicity). The horizontal green line corresponds to $\kappa_1 = 0.070$, and the black one to $\kappa_u = 1/12$.

In the focal region of a future earthquake the stress gradually changes *before* failure. It is commonly accepted that, after the mainshock occurrence, the stress value reduces to a smaller value, a fact, however, which is not fully captured by the simple BK model considered here. In other words, in the steady SOC state of this model the system has an average f_l value, $\bar{f}_l$, around $\bar{f}_l = 0.8785$ that remains almost constant (i.e., practically within 0.0055) after the occurrence of any avalanche (cf. $X(i)$ in Fig. 8.1). Our computations reveal (see Fig. 8.3) that when considering a reasonable decrease, e.g., by a few percent, of $\bar{f}_l$, the system exits the steady SOC state and then returns to it through a transient in which the κ_1 value scatters around 0.070, similarly to that depicted in Fig. 8.1. This can be seen in Fig. 8.3, which depicts the results that show what happens with κ_1 when reducing each f_l by 1% (a), 2% (b) and 10% (c) of its value at SOC. The κ_1 value is given here in red while magenta corresponds to one standard deviation $\pm\sigma$. A reasonable reduction of f_l may be around a few percent at the most (see especially Fig. 8.3(a) and 8.3(b)). The results have been obtained by means of the Monte Carlo procedure described

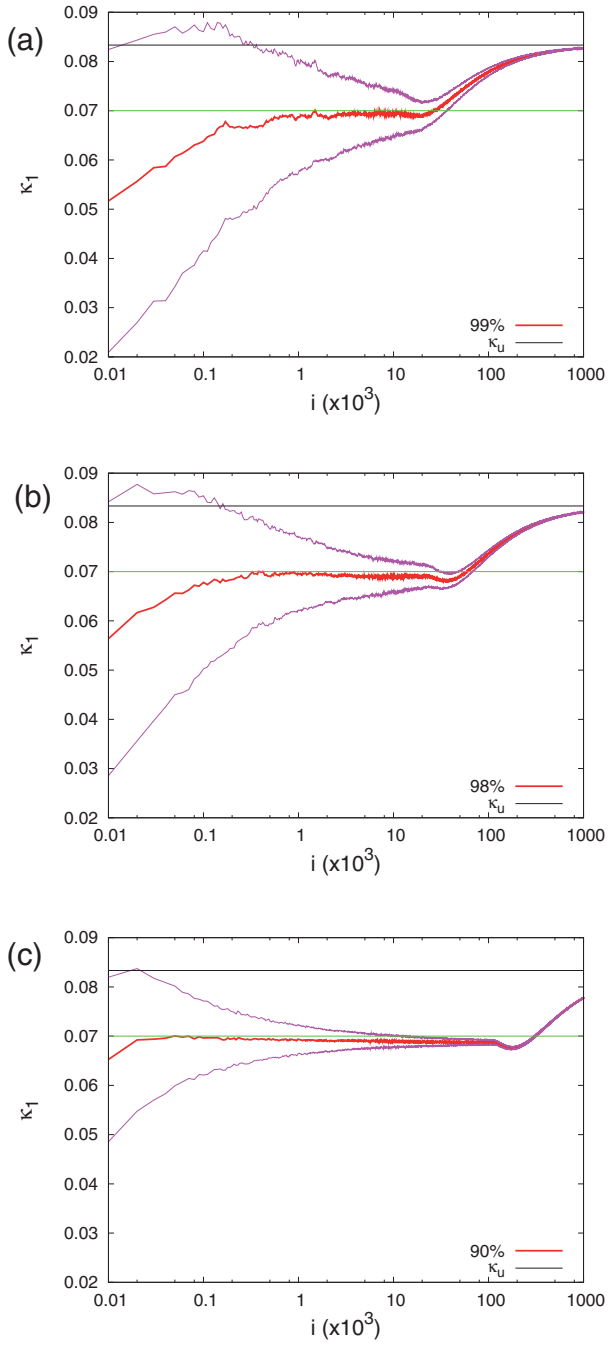

Fig. 8.3 Results showing the behavior of the average value of κ_1 (red) when decreasing $\bar{f}_l$ to (a) 99%, (b) 98% and (c) 90% of its value at SOC. The results have been obtained as follows. We considered 10^3 systems with the initial f_l values randomly scattered around $f_0 = 0.87$. Each system was driven to SOC and in order to obtain a reliable series f_{lSOC}, $l = 1, 2, \ldots L$, the first 10^7 avalanches were ignored in natural time analysis. Then, each of these f_l values was reduced to 99%, 98% and 90%, respectively, of its value at SOC, i.e., f_{lSOC}, and natural time analysis was initiated ($i = 0$). The magenta curves depict the one standard deviation($\pm\sigma$) interval. The horizontal green line corresponds to $\kappa_1 = 0.070$, and the black one to $\kappa_u = 1/12$. Taken from Ref. [82].

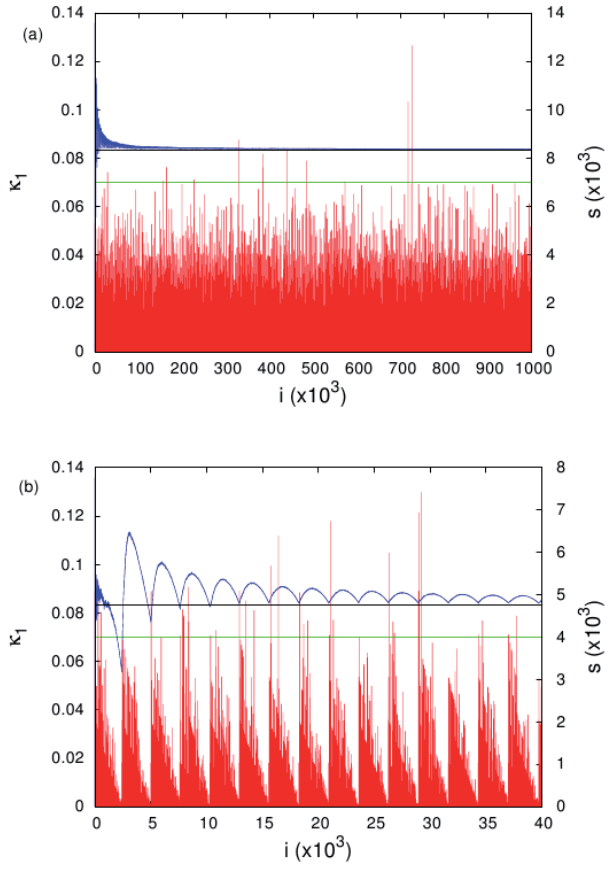

Fig. 8.4 The results obtained when using, instead of the periodic function $\Psi(x)$, the strictly non-increasing function $\phi(x) = \frac{(2-\delta f)^2/a}{x+(2-\delta f)/a} - 1$, introduced in Ref. [57]. The parameters $L = 1024$, $a = 4$, $f_0 = 0.87$ and $\delta f = 0.1$ are the same as those in Figs. 8.1 and 8.2. Results are given for 10^6(a) and 40,000(b) avalanches. The quantities shown here are the same as those plotted in Fig. 8.2. The horizontal green line corresponds to $\kappa_1 = 0.070$, and the black one to $\kappa_u = 1/12$. As shown in (b), the avalanche size $s(\equiv Q_k)$ is quasi-periodic, leading to κ_1 values "oscillating" close to (but mostly higher than) κ_u.

in the caption of this figure. Hence, the value $\kappa_1 = 0.070$ *can be considered as quantifying the extent of the organization of the complex system at the onset of the critical stage.*

We emphasize that such a behavior is not observed for a variant of the model which *does not* exhibit SOC [76], e.g., when using, instead of a periodic function $\Psi(x)$, the strictly non-increasing function $\phi(x)$ introduced by Nakanishi [57] (see Fig. 8.4). This figure shows the results, in a similar fashion to those depicted in Fig. 8.1, obtained from the model when using, instead of the periodic function $\Psi(x)$, the strictly non-increasing function introduced by Ref. [57]. In this case the behavior of κ_1 is found to be distinctly different from that of the SOC model depicted in Fig. 8.1 as well as in Fig. 8.2.

In summary, natural time analysis was made for a one-dimensional SOC model introduced to describe avalanches in stick–slip phenomena. It belongs to the same universality class as the "train" model for earthquakes suggested by Burridge and Knopoff. We found that the value $\kappa_1 = 0.070$ can be considered as quantifying the extent of the organization of the complex system at the onset of the critical stage.

8.3 Natural time analysis of the Olami–Feder–Christensen (OFC) earthquake model

8.3.1 The Olami–Feder–Christensen model. Introduction

The OFC model originated by a simplification of the Burridge & Knopoff spring-block model [14] by mapping it into a non-conservative cellular automaton, simulating the earthquake's behavior and introducing dissipation in the family of SOC systems. In the spring-block model, which as mentioned in § 8.2.1 consists of a two-dimensional array of blocks in a flat surface, each block is connected (by elastic springs) with its neighbors, and in the vertical direction, to a driving plate which moves horizontally at velocity v. When the force acting on a block overcomes the static friction with the surface, the block slips. In the OFC model the force on a block is stored in a site of a square lattice, and the static friction threshold is assumed to have the same value over all blocks. If force input occurs in discrete steps instead of continuous and if thresholds are random but not quenched, quasi-periodicity emerges combined with power laws [65].

The criticality of the OFC model has been debated [21, 54]. Also, the SOC behavior of the model is destroyed upon introducing some small changes in the rules of the model, e.g., replacing open boundary conditions with periodic boundary conditions [64], introducing frozen noise in the local degree of dissipation [56] or in its threshold value [43], including lattice defects [23]. Despite these findings as well as others which show [61], that it is insufficient to account for certain aspects of the *spatiotemporal* clustering of seismicity, the OFC model appears to show many features found in real earthquakes. As far as earthquake predictability [62] or Omori law [39, 36] are concerned, the OFC model appears to be closer to reality than others [85]. In addition, for certain values of the local degree 'α' of dissipation (i.e., if 'α' is chosen above 0.17, see also below), the OFC model exhibits avalanche size distribution that agrees well [52] with the Gutenberg–Richter (G-R) law; see Eq. (6.1). These are some of the reasons why the OFC model is considered to be the prime example [5] for a supposedly SOC system for earthquakes but the question of whether real earthquakes are described or not by SOC models of this type, or whether other kinds of mechanisms, e.g., Refs. [51, 50], need to be involved, remains unsolved [9, 86, 39, 36, 65]. Note also that an analysis of the OFC model in the nonextensivity framework (Section 6.5) has been made by Caruso et al. [20] and further discussed in Ref. [69].

Description of the Olami–Feder–Christensen (OFC) model. The OFC model [59] runs as follows: we assign a continuous random variable $z_{ij} \in (0,1)$ to each site of a square lattice, which represents the local 'energy'. Starting with a random initial configuration taken from a uniform distribution in the segment (0,1), the value z_{ij} of all sites is simultaneously increased at a uniform loading rate until a site ij reaches the threshold value $z_{thres} = 1$ (i.e., the loading Δf is such that $(z_{ij})_{max} + \Delta f = 1$). This site then topples which means that z_{ij} is reset to zero and an 'energy' αz_{ij} is passed to every nearest neighbor. If this causes a neighbor to exceed the threshold, the neighbor topples also, and the avalanche continues until all $z_{kl} < 1$. Then the uniform loading increase resumes. The number of topplings defines the size s of an avalanche or "earthquake". This is the quantity that is used as Q_k in the natural time analysis. The coupling parameter α can take values from zero to 0.25. Smaller α means more dissipation, and $\alpha = 0.25$ corresponds to the conservative case.

The parameter α is the *only* parameter of the model, apart from the system size L, the edge length of the square lattice. Except from the initial condition the model is deterministic. The model can be supplemented by open boundary conditions (OBC) in which the sites at the boundary distribute energy to the outer sites, which cannot topple, thus energy is removed at the boundary. Another possibility, is to use free boundary conditions (FBC). In this case, α varies locally

$$\alpha_{ij} = \frac{1}{n_{ij} + K}. \tag{8.1}$$

where n_{ij} is the actual number of nearest neighbors of the site ij. For sites in the bulk $n_{ij} = 4$, for sites at the edges $n_{ij} = 3$ and for the four sites at the corners $n_{ij} = 2$. The symbol K denotes the elastic constant of the upper leaf springs measured relatively to that of the other springs between blocks [36]. Obviously the OFC model is non-conservative for $K > 0$ for which $\alpha_{ij} < 0.25$ in the bulk. Finally, periodic boundary conditions (PBC) can be imposed but these destroy [64] criticality. Except in the case of PBC, the sites at the boundary receive energy only from three or two neighbors, and therefore topple on average less often than sites in the interior, which leads to the formation of "patches" of sites with similar energy. This patch formation proceeds from the boundaries inward [53, 29]. Due to the dynamics of the model, there occur avalanches of all sizes. The mechanism producing these avalanches are different on different scales [29]. Large avalanches are mainly patch-wide avalanches, while smaller avalanches occur between patches and constitute a series of 'foreshocks' or 'aftershocks' [39]. Also, avalanches at different distances from the boundaries have different sizes.

As already mentioned, there has been no agreement as to whether the model is indeed critical for all values of the coupling or only in the conservative case [21, 22, 54]. In particular, detailed analytical studies [13, 24] for a *random-neighbor* version of the OFC model concluded that *only* in the conservative limit the model becomes critical (this conclusion was also shared by de Carvalho and Prado [21]). Furthermore, using a variety of arguments and large-scale computer simulations, the most exhaustive analyses [10, 35, 85, 5] coincide to the conclusion that the spatially extended version of the non-conservative OFC model is *not* critical.

Thus, the state of the art is [9] that the OFC model is *not* truly scale-invariant except for its conservative limit.

8.3.2 Natural time analysis of the Olami–Feder–Christensen model

8.3.2.1 Results in the transient and the stationary regime of the OFC model

We first present the results [68] for the transient regime of the OFC model using the quantity $f = \sum(\Delta f)$, which represents the total increase of z_{ij} due to the external force loading in each site. Since the loading rate is assumed uniform in time, *f plays a role analogous to that of the conventional time T*, i.e., $T \equiv f$.

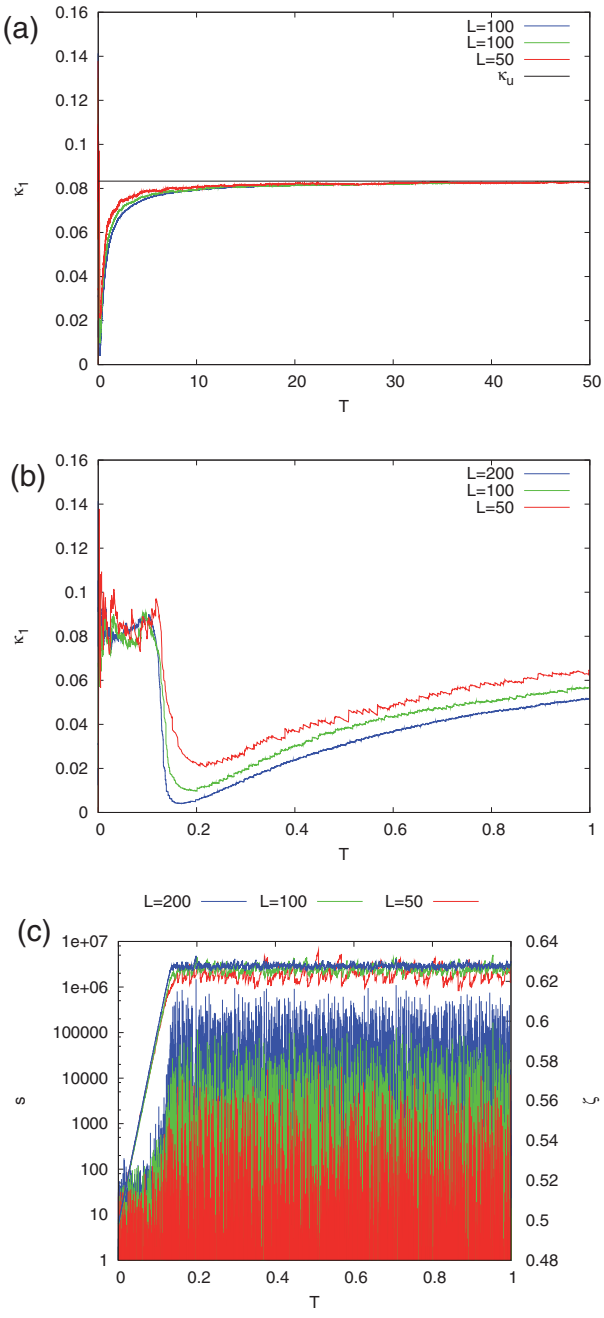

Fig. 8.5 The conservative case of the OFC model for various L ($= 50, 100, 200$) and OBC: (a) κ_1 versus the 'time' T; (b) an excerpt of (a) showing the transient regime; (c) the avalanche size s (left scale) and the mean energy ζ (right scale) versus the 'time' T.

We find that the conservative and non-conservative cases of the OFC model display a qualitatively different behavior.

In the former case, as can be seen in Figs. 8.5(a),(b) which depict the evolution of κ_1 versus the 'time' T, the quantity κ_1 exhibits a *single* transient consisting of an abrupt decrease, from a value larger than κ_u down to $\kappa_1 \approx 0$ (for larger L see Fig. 8.6), and then κ_1 gradually increases up to the value $\kappa_u = 1/12$. The latter value reflects that the system has reached a steady state, thus the κ_1 value approaches that of the "uniform" distribution. Note that, as the number of avalanches taken into account in the κ_1-calculation increases, the contribution of the avalanches in the transient regime to the κ_1 value becomes gradually smaller compared with that of the avalanches in the stationary regime. In addition, we note that the number of avalanches corresponding to the minimum value of κ_1 was found to scale with L^2. This is reminiscent of the scaling found in Ref. [22] when plotting the mean 'energy' per site $\zeta = \sum z_{ij}/L^2$ versus the number of avalanches. The use of the 'time' T which is *intensive* and *not extensive* quantity, as does the number of avalanches, simplifies the study of this transient. By investigating the κ_1 versus T curves for various L and examining their behavior close to $\kappa_1 \approx 0$, we find (see Fig. 8.6) that all these curves

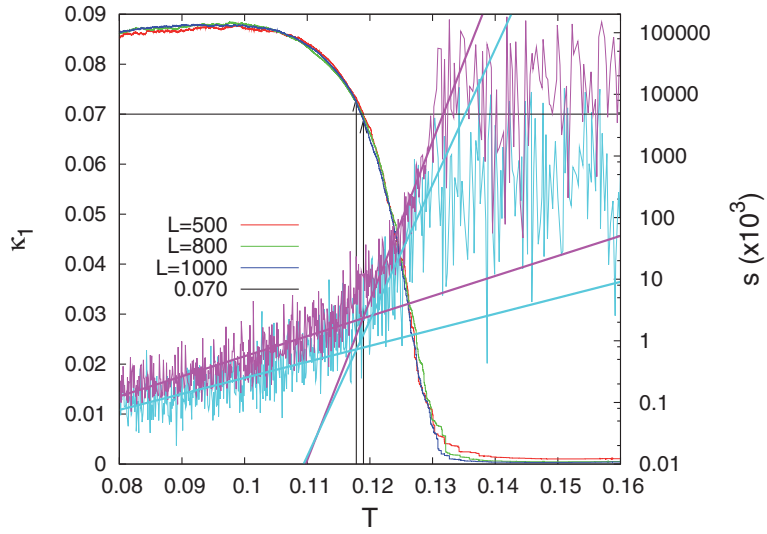

Fig. 8.6 The collapse of various κ_1 vs T curves for the conservative case of the OFC model onto a single curve upon varying the size of the system $L = 500$ (red), 800 (green), 1000 (blue). In the left vertical scale we depict κ_1, while in the right the avalanche size s for $L = 500$ (cyan) and $L = 1000$ (magenta). The cyan (magenta) line corresponds to the maxima observed every 30 (100) avalanches. The thick straight lines correspond to their exponential fits for $T \in [0.08, 0.11]$ and $T \in [0.12, 0.131]$ (note that $T = 0.131$ is approximately the value at which the linear increase of ζ ceases, see Fig. 8.5(c)), and exhibit a cross-over during which the slope increases by one order of magnitude. The arrows show the values of κ_1 corresponding to the points at which the two linear fits (of the same color) intersect. The horizontal black line corresponds to $\kappa_1 = 0.070$.

collapse onto a single curve. Figure 8.5(c) depicts the size s of avalanches versus T along with the mean energy ζ. We observe that the almost abrupt decrease of κ_1 is due to the drastic (exponential) increase by several orders of magnitude of the avalanche size s when ζ approaches its steady state value. This exponential increase is better visualized in Fig. 8.6 where, for the sake of clarity, we depict for $L = 500(1000)$ the maximum avalanche size deduced every 30(100) avalanches versus T (cf. the two values 30 and 100 are considered to account for the fact that the larger system exhibits more avalanches for the same increase in T). One can recognize roughly three linear regions (only two of which are fitted with straight lines in Fig. 8.6, for the sake of clarity) in this log-linear plot (right scale). The first one corresponds to the region $T \in [0.08, 0.11]$ during which the (maximum) avalanche size increases by almost one order of magnitude (see the lower thick solid lines in Fig. 8.6). The second stage corresponds to an almost abrupt later increase by almost five orders of magnitude during $T \in [0.12, 0.131]$, which is linear in the log-linear plot, see the steeper thick solid lines in Fig. 8.6. After $T = 0.131$, which is the value at which the initial linear increase of ζ ceases, see Fig. 8.5(c), the (maximum) avalanche size does not exhibit any obvious trend, thus making unnecessary the plot of the corresponding fits in Fig. 8.6.

The non-conservative case gives a more complicated feature, see Fig. 8.7, because the aforementioned single transient of the conservative case now splits into two parts. Figures 8.7(a),(b) depict the evolution of κ_1 versus T for $\alpha = 0.24$ for various lattice sizes. In Fig. 8.7(b), which is an excerpt of Fig. 8.7(a), an abrupt decrease of κ_1 is observed at $T \approx 0.3$, accompanied by a peak of ζ (see Fig. 8.7(c)) centered at $T \approx 0.16$, which for large L does *not* depend on L. This κ_1 decrease is followed by an increase – coming from a decrease of s (see Fig. 8.7(c)) – and κ_1 reaches a maximum which is subsequently followed by a gradual decrease down to a minimum. This second minimum is observed at $T \approx 1$ for $L = 50$, $T \approx 5$ for $L = 100$ and $T \approx 25$ for $L = 200$, thus indicating that it scales somewhat faster than L^2, which deviates from the finite-size scaling found for the single minimum of the transient in the conservative case. Note that the finite-size scaling observed during the first part of the transient could be attributed to an almost one order of magnitude exponential increase of s when T varies approximately in the range $[0.10, 0.20]$ (see Fig. 8.7(c) and Fig. 8.8(a)) which is similar to the one observed in the conservative case when $T \in [0.08, 0.11]$ (see Fig. 8.8(b)). The dissipation, however, does not allow the emergence of the second much more significant exponential increase of s observed in the conservative case (see the steeper thick solid lines in Fig. 8.6 and the insets of Fig. 8.8). This might be the reason for which the simple finite-size scaling found for $T \in [0.10, 0.20]$ ceases at later times T. The apparent similarity of the first transient stages observed for $T \in [0.08, 0.11]$ and $T \in [0.10, 0.20]$ for the conservative (e.g. Fig. 8.8(b)) and non-conservative cases (e.g. Fig. 8.8(a)), respectively, could be understood as follows. Figure 8.8 shows the T-dependence of the percentage P_{vis} (red solid lines) of the sites "visited" by the OFC toppling rule, which *'diffuses'* energy to the nearest neighbors. We observe that in both cases a similar exponential increase starts when P_{vis} approaches the value of the site *percolation* threshold p_c ($p_c = 0.59274598(4)$; see Ref. [49]) for the two-dimensional square lattice. Thus, when the "visited" sites begin to percolate through the square lattice, the two cases exhibit a similar behavior irrespective of the energy conservation. It seems that the interplay between the diffusive character of the OFC toppling rule and the geometrical phenomenon of percolation is dominating at this stage. Recall

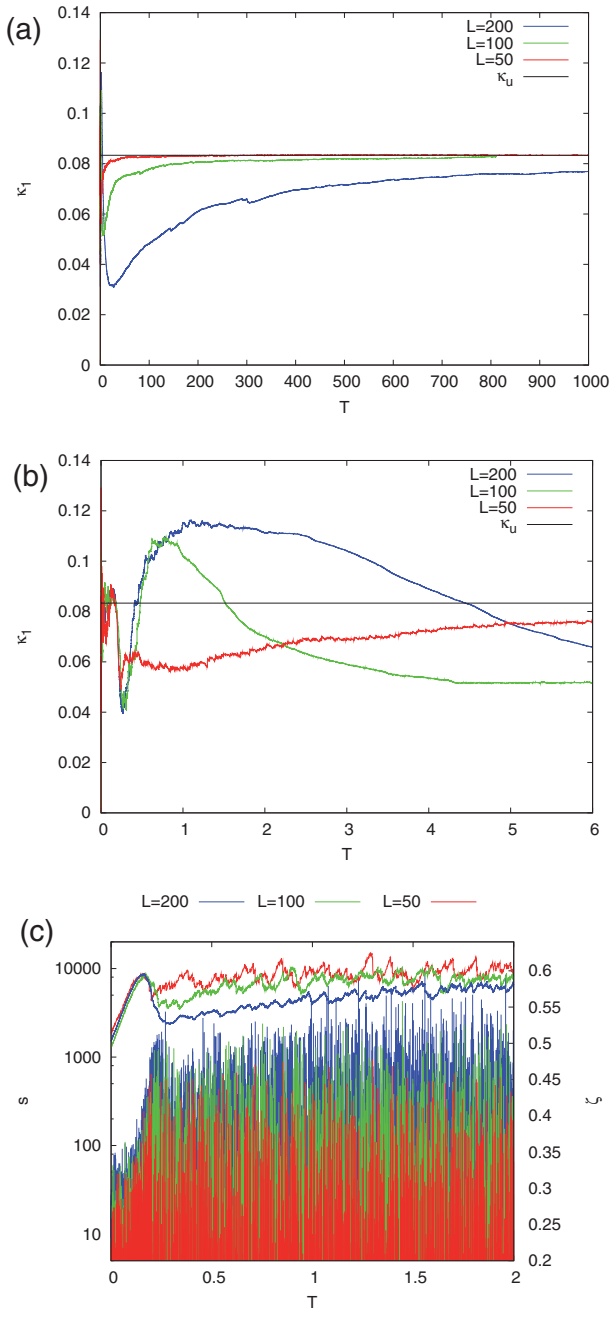

Fig. 8.7 The non-conservative ($\alpha = 0.24$) case of the OFC model for various L ($= 50, 100, 200$) and OBC: (a) κ_1 versus the 'time' T; (b) an excerpt of (a) showing the transient regime; (c) the avalanche size s (left scale) and the mean energy ζ (right scale) versus the 'time' T.

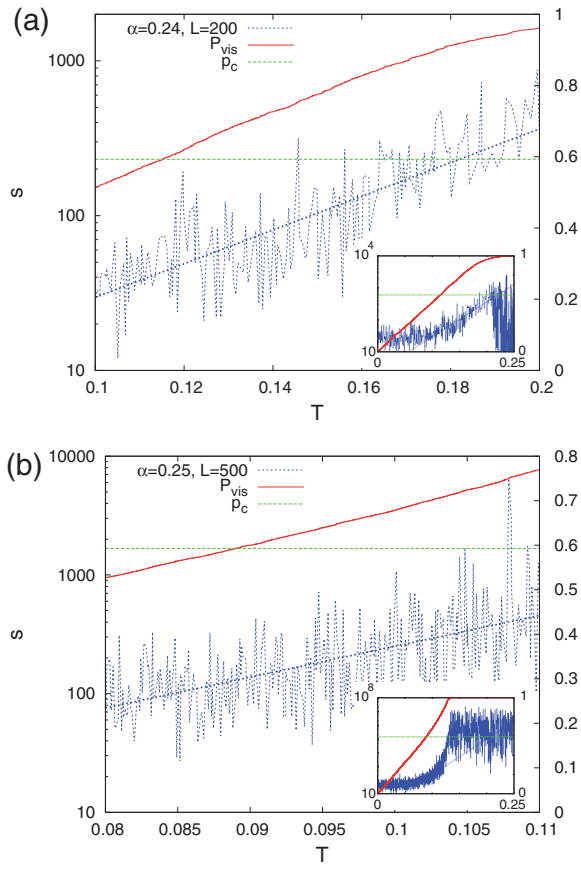

Fig. 8.8 (a): The (blue) dotted broken lines depict the maximum avalanche size observed every 20 avalanches versus T for the non-conservative case ($\alpha = 0.24$) for $L = 200$. The straight thick (blue) dotted line shows a linear fit in the log-linear plot for $T \in [0.1, 0.2]$. (b) is the same as (a), but every 30 avalanches for the conservative case ($\alpha = 0.25$) for $L = 500$ and $T \in [0.08, 0.11]$. Using the right scales in both (a) and (b), we also show the percentage P_{vis} (red solid lines) of the sites "visited" by the OFC toppling rule versus T together with the site-percolation threshold [49] $p_c = 0.59274598(4)$ (green dashed horizontal line) for the two-dimensional square lattice. The whole picture for $T \in [0, 0.25]$ is reproduced in the insets.

that an "unvisited" site of low or moderate random initial 'energy' $(z_{ij})_0$ will be toppled if it receives, apart from the overall increase of $\sum(\Delta F)(= T)$, enough energy to exceed the threshold due to the energy that has diffusively arrived at the site from another site (of possibly higher initial 'energy' $(z_{i'j'})_0$). During this stage it is reasonable to assume that the energy δz arriving at an "unvisited" site reaches it through a single path. Thus, the amount δz scales as α^n, where n is the (presumably small) number of the sites in the path. This amount is not significantly affected whether $\alpha = 0.24$ or $\alpha = 0.25$ and this is why the conservative and the non-conservative cases resemble each other. Later, as the visited sites cluster, the differences emerge dramatically: the energy loss in the non-conservative case occurs at all points of the lattice ($\propto L^2$) thus destroying finite-size scaling, whereas in the conservative case the clusters formed do not alter the finite-size scaling since the energy loss occurs only at the boundaries ($\propto L$) of the system. Returning, now to the κ_1 behavior, we observe the following:

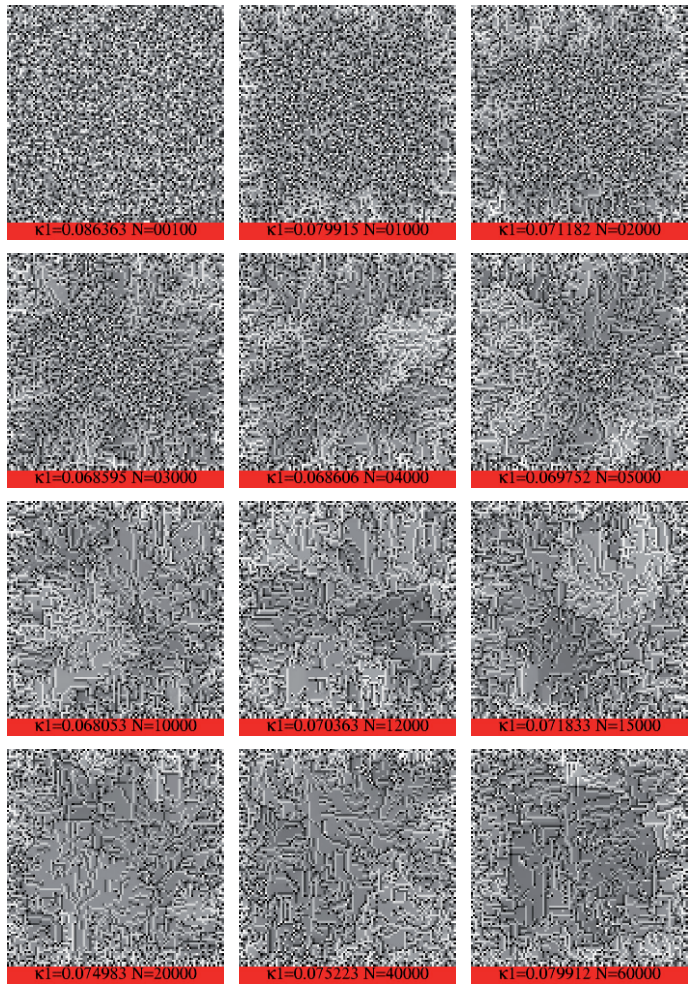

Fig. 8.9 Snapshot images of the strain field in the OFC model ($L = 100$ and $a = 0.22$, OBC), showing that the coherent structure formation is accompanied by values of κ_1 close to 0.070. Here only avalanches with $s > 10$ are considered in natural time analysis and N corresponds to the number of such avalanches. The grey scale (black to white) corresponds to the values of z_{ij} (zero to unity).

After the second minimum, κ_1 increases *slowly* up to the value κ_u. It is during this increase that a prolonged period exists in which coherent domains of the z_{ij} field (strain field) are developed in the non-conservative case; see Fig. 8.9.

Recall that Figs. 8.5 and 8.7 have been drawn by considering all avalanches generated, i.e, $Q_k = s_k \geq 1$. Similar natural time analysis, however, can be performed upon adopting an avalanche size threshold s_0 (i.e., an avalanche of size s is considered as an event in natural time only if $s > s_0$).

Selecting an appropriate threshold s_0 relative to the edge length L, we can find κ_1 values that scatter around 0.070 when the aforementioned coherent structures in the strain field start to appear in the non-conservative case. Such an example is shown in Fig. 8.9 in which a threshold $s_0 = 10$ was selected for $L = 100$ and $\alpha = 0.22$.

Recapitulating the aforementioned results in the transient regime, we see that when comparing the conservative and non-conservative cases, they exhibit considerable differences on how they move away from the initial random state. The question is raised, however, of whether some of these differences can shed light on which of these behaviors is critical and the other not. An answer can be provided on the basis of the following two key differences related to the curves κ_1 versus T and ζ versus T. First, let us consider the κ_1 versus T behavior. In the conservative case, when studying the system for various system sizes L and focusing on the behavior close to $\kappa_1 \approx 0$, we observe, as mentioned, that all the κ_1 vs T curves collapse onto a single curve (see Fig. 8.6).

In addition, in the conservative case, the value $\kappa_1 \approx 0.070$ (that occurs at $T = 0.119$) is accompanied by an abrupt exponential increase of the avalanche size s, which is indicative of the approach to a critical behavior; see the arrows in Fig. 8.6 that mark the cross-over points between the aforementioned log-linear fits (thick straight lines) of the (maximum) avalanche size.

It is this drastic increase of s – by several orders of magnitude – which leads to a κ_1 decrease down to $\kappa_1 \approx 0$ and then κ_1 gradually increases reaching the value $\kappa_u = 1/12$ in the stationary regime. On the other hand, in the non-conservative case the curves κ_1 vs T obtained upon increasing the system size L, do *not* collapse onto a single curve (see Fig. 8.7(b), where it is evident that the second part of the transient does not coincide for different L). Second, let us now consider the ζ vs T behavior: In the conservative case; Fig. 8.5(c) shows that the curves of the mean energy ζ upon studying different L collapse onto a single one after the exponential increase of s (subsequent to the appearance of $\kappa_1 \approx 0.070$ mentioned above). Such a collapse in the ζ vs T curves, however, is not observed in the non-conservative case, see Fig. 8.7(b) (note that in this case, Fig. 8.7(c), the s vs T curve exhibits an increase of only around one order of magnitude in contrast to the several orders of magnitude increase of the conservative case mentioned above).

We now summarize the behavior in the transient regime. *Only in the conservative case* when studying κ_1 vs T and/or ζ vs T (recall that the quantities κ_1, T and ζ are intensive and *not* extensive) the curves obtained upon varying the system size L collapse onto a single curve, as it should for a *critical* system. This is *not* observed in the non-conservative case, meaning that a larger system needs larger T to reach the 'steady-state' ζ value. This points to (the absence of a thermodynamic limit, and hence to) *non-criticality*.

As for the stationary regime, for both the conservative and the non-conservative cases, the κ_1 value stabilizes at a value around $\kappa_u = 1/12$, see Figs. 8.5(a) and 8.7(a), which as mentioned reflects that the system has reached a steady state.

8.3.3 The predictability of the OFC model based either on the mean energy or on the interrelation between the κ_1 value and the exponent of the inverse Omori law

Here, in order to study the predictability of the OFC model which has been attributed to the occurrence of 'foreshocks' (note that 'aftershocks' have been also observed) in the non-conservative case of the model [39], we start with a prediction algorithm motivated by the one used by Zhang et al. [88]. This algorithm was inspired by an earlier one proposed by Keilis-Borok and coworkers [46, 45] and by Pepke and coworkers [62, 63]. In particular, we consider the mean 'energy' ζ which is a function of the 'time' T. For this function, the time increased probability (TIP) is turned on when $\zeta > \zeta_c$, where ζ_c is a given threshold in the prediction. If the size s of the next avalanche is greater than a target avalanche size threshold s_c, we have a successful prediction. For binary predictions, the prediction of events becomes a classification task with two type of errors: missing an event and giving a false alarm. We therefore choose, in a similar fashion as in § 6.4.2, the receiver operating characteristics (ROC) graph [30] to depict here the prediction quality. As an example, the ROC graph for $L = 100$ and $K = 2$ is shown in Fig. 8.10, where the various curves correspond to various values of s_c increasing from the bottom to the top. Recalling from § 6.4.2 that the diagonal line in such a plot corresponds to random predictions, and the points in each curve lie above it (meaningful predictions), we conclude that the precursory function ζ results in meaningful prediction which becomes very robust for larger values of s_c. We note, however, that the selection of the mean energy ζ as a precursory function suffers from the drawback that in the case of earthquakes the measurement of this quantity is dif-

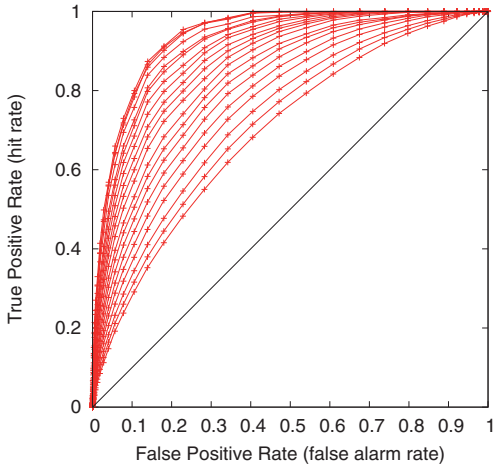

Fig. 8.10 Receiver operating characteristics graph for the OFC model with $L = 100$ and $K = 2$ when using the mean energy ζ as a predictor: the true positive rate (hit rate) versus the false positive rate (false alarm rate) for various s_c values increasing from the bottom ($s_c = 361$) to the top ($s_c = 1{,}938$) with constant steps.

ficult in practice and indirect (what can be measured by some techniques is the increment of stress or strain *not* the absolute values themselves [88]).

The occurrence of 'foreshocks' (f) as well as 'aftershocks' (a) in the OFC model has been exhaustively studied by Helmstetter et al. [36]. Here, we solely focus on the former (foreshocks) that are described by the so-called inverse Omori law [38, 36] which states that the average increase of seismicity observed at the time t before the occurrence time t_c of a mainshock is given by

$$N_f(t) = \frac{K_f}{(t_c - t + c)^{p_f}} \tag{8.2}$$

where the subscript "f" refers to the foreshocks and the quantities K_f and c are taken constants. The inverse Omori exponent p_f is usually close to or slightly *smaller* than the corresponding exponent p_a of the usual Omori law for aftershocks [37] (see also Section 6.1). Helmstetter et al. [36] defined as a "mainshock" (see their definition $d = 0$) any earthquake of magnitude m which was not preceded or followed by a larger earthquake in a time window of length $T(m)$ equal to 1% of the average return time of an earthquake of magnitude m. Foreshocks are then selected as all earthquakes occurring within the time $T(m)$ before a mainshock. The value of p_f has been found [37] by averaging the seismicity rate before a large number of mainshocks, because there are huge fluctuations of the rate of seismicity before individual mainshocks. Helmstetter et al. [36] generated synthetic catalogs with the OFC model and determined the p_f value using various lattice sizes L and K values, see their table I. They studied the cases for $K = 0.5$, 1, 2 and 4, i.e., for bulk $\alpha = 0.222$, 0.2, 0.167 and 0.125, and among the results presented in their table I, we only focus here on the larger lattice sizes, i.e., $L = 1024$ and $L = 2048$. The average value of these p_f exponents results equal to $p_f = 0.72$, if we consider all the relevant p_f values that correspond [36] to b values ranging from $b = 0.67$ to $b = 0.92$. If we restrict ourselves, to those p_f values corresponding to more reasonable values of b, e.g., $b \geq 0.76$, we find that the average p_f value increases somewhat to $p_f = 0.78$. These average p_f values (0.72 and 0.78) suggest that p_f may be considered to be around $p_f \approx 0.75$, which is just the p_f value given in their Fig. 2 for a synthetic catalog generated [36] with $L = 2048$ and $K = 2$. The power law form of the inverse Omori law, i.e., Eq. (8.2), implies that in natural time

$$p(\chi) = \frac{1 - p_f}{(1 - \chi)^{p_f}} \tag{8.3}$$

which reflects an increase of foreshocks as we approach the mainshock at $\chi = 1$. Equation (8.3), when substituted into Eq. (2.97) for the estimation of the variance κ_1 of natural time, leads to

$$\kappa_1 = \frac{2}{(2 - p_f)(3 - p_f)} - \frac{1}{(2 - p_f)^2} \tag{8.4}$$

The κ_1 values determined from Eq. (8.4) are plotted versus p_f in Fig. 8.11. At the same plot, the two κ_1 values that correspond to the aforementioned average p_f values (i.e., $p_f = 0.72$ and $p_f = 0.78$) are marked, which scatter around $\kappa_1 \approx 0.070$. This κ_1 value is comparable with the one ($\kappa_1 \approx 0.070$) determined when analyzing in natural time the small seismic events that occur after the initiation of a SES activity and before the occurrence of a mainshock (see Chapter 7). In other words:

The 'foreshocks' associated with the non-conservative OFC model give on the average a κ_1 value which is more or less comparable with that ($\kappa_1 \approx 0.070$) obtained from the analysis of the real seismic data that precede mainshocks.

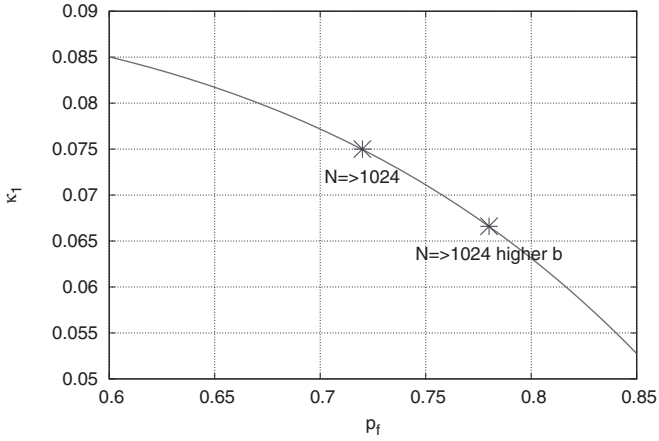

Fig. 8.11 The values of κ_1 vs the power law exponent p_f according to Eq. (8.4). The two points marked correspond to the two average p_f values discussed in the text.

We note, however, that this property of κ_1 is difficult to be used for the prediction of the avalanches in the OFC model in a way similar to that used for ζ. The reason is that the mean energy ζ solely depends on the current state of (the z_{ij} field of) the system, whereas κ_1 reflects the history of the system as it evolves starting from some (initial) state. Thus, the application of κ_1 for prediction purposes in the OFC model requires the real-time identification of the initiation of the foreshock time series. The latter is extremely difficult. Recall that in the field experiments, it is the initiation of the SES activity which signifies that the stress has reached a critical value (see § 1.6.2) in the preparatory volume; then, the identification of a "critical" time series, by employing the method explained in Chapter 7, allows the determination of the occurrence time of the impending strong earthquake.

8.3.4 The predictability of the OFC model on the basis of the change ΔS of the entropy in natural time under time reversal

Here, we focus on what happens before the occurrence time T_0 of a large avalanche during the stationary regime of the non-conservative case of the OFC model by employing the change ΔS of the entropy in natural time under time reversal (Section 3.5). In particular, for each large avalanche, we study the time evolution of ΔS_l (see § 3.5.1) obtained from the preceding avalanches time series. Following the study of foreshocks in Ref. [36] and in view of the fact that, as mentioned in § 8.3.3, there are huge fluctuations before individual large avalanches, our results have been found by averaging the values obtained before an appreciably high number of large avalanches. For example, Fig. 8.12 depicts the

results for the average change ΔS (left scale) of the entropy in natural time under time reversal and the average value of the mean energy ζ (right scale) obtained by using the last 1,000 avalanches (irrespective of their size) before large avalanches of size $s \geq 100$ (red), 1,000 (green) and 2,000 (blue) in the non-conservative OFC model with $L = 100$ and $K = 2$. In the horizontal axis, the time is measured from the occurrence time T_0 of the large avalanche. We find that ΔS_l minimizes (note that. $|\Delta S_l|$ maximizes) *before* the impending large avalanche, thus signaling the imminent major event. The negative values of ΔS reflect, through Eq. (3.79), that the avalanche size tends to increase as the time approaches that of the large avalanche, "mainshock" (due to the foreshocks, mentioned in the previous subsection, that start to become discernable from the background "seismicity"). Furthermore, note that ΔS changes sign, becoming negative, when the parameter ζ almost starts to increase (recall that the quantity ζ, as shown in § 8.3.3, can be used as a predictor for the large avalanches).

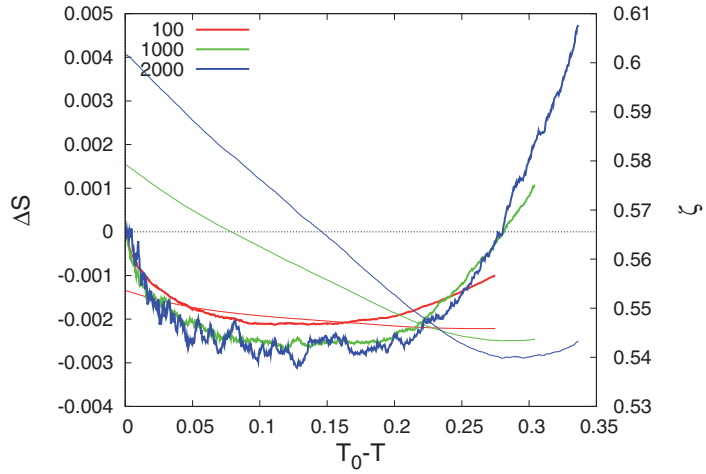

Fig. 8.12 Results from averaging the last 1,000 events before a large avalanche ($s \geq 100$, 1,000, 2,000 occurring at T_0) in the OFC model with $L = 100$ and $K = 2$: the change ΔS (left scale, thick lines) of the entropy in natural time under time reversal and the mean energy ζ (right scale, thin lines) as a function of the 'time' $(T_0 - T)$ to the large avalanche. Note that ΔS minimizes *before* the occurrence time T_0 of the large avalanche, and changes sign when ζ almost starts to increase.

Proceeding one step further, Fig. 8.13 depicts the ROC graph when using $\overline{\Delta S}$ as a predictor. In this calculation, $\overline{\Delta S}$ was determined as the average value of ΔS_l using the (past) events that occurred within the time period $T_{now} - T = 0.05$ to 0.2, where T_{now} stands for the present time. This $\overline{\Delta S}$ is used as a predictor for the size of the next avalanche (in the sense described above in § 8.3.3; see also § 6.4.2). The results (red curves) lie above the diagonal and are statistically significant when compared with the cyan curves that correspond to the extrema of 100 trials obtained when performing the same calculation by using *randomly* shuffled $\overline{\Delta S}$ values. These results are certainly less impressive than those

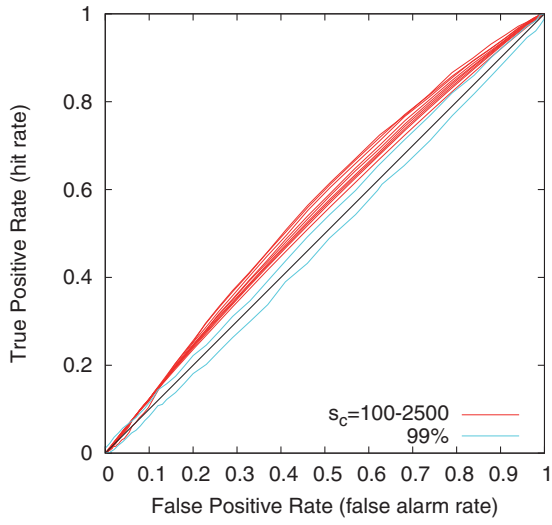

Fig. 8.13 Receiver operating characteristics graph (red) for the non-conservative OFC model with $L = 100$ and $K = 2$ when using $\overline{\Delta S}$ as a predictor (i.e., the TIP is on when $\overline{\Delta S}$ becomes less than some threshold): The true positive rate (hit rate) versus the false positive rate (false alarm rate) for various s_c values increasing from the bottom ($s_c = 100$) to the top ($s_c = 2{,}500$) with constant steps. The cyan curves depict the extrema obtained when repeating 100 times the same calculation using a random predictor (see the text).

in Fig. 8.10, but we emphasize that the predictor here is *solely* based on the sizes of the past avalanches.

8.3.5 Summary of the results

The main conclusions of the natural time analysis of the time series of avalanches in the OFC model could be summarized as follows.

First, concerning the transient period: the behavior is different depending on whether the model is conservative ($\alpha = 0.25$) or non-conservative ($\alpha < 0.25$). In the former case, there is a *single* transient which mainly consists of an abrupt decrease of the variance κ_1, down to a minimum $\kappa_1 \approx 0$ and then a gradual increase up to the value $\kappa_u = 1/12$ of the "uniform" distribution.

Before this minimum, the κ_1 vs T curves deduced for various system sizes ($L \geq 500$) *collapse* onto a single curve and when the κ_1 value reaches $\kappa_1 = 0.070$ (at around $T = 0.119$), an abrupt exponential increase of the avalanche size s occurs signaling the approach to the *critical* behavior.

It is this drastic increase of s which decreases the κ_1 value to $\kappa_1 \approx 0$ (the number of the generated avalanches corresponding to the minimum value $\kappa_1 \approx 0$ is found to scale with L^2). On the other hand, in the non-conservative case, the transient period splits into two parts. In the first part, the number of avalanches corresponding to the minimum κ_1 value does scale with L^2, but in the second part it increases much more quickly. During the second part, coherent domains of the strain field gradually develop. This coherent structure formation is accompanied by κ_1 values close to 0.070.

Second, the resulting power law exponent p_f of the inverse Omori law for the 'fore-shocks' identified in the non-conservative cases for large lattice sizes ($L \geq 1024$), is shown to correspond to κ_1 values scattered around $\kappa_1 \approx 0.070$.

Third, there exists a nonzero change ΔS of the entropy in natural time under time reversal, thus signaling the breaking of the time symmetry and reflecting predictability in the OFC model.

8.4 Explanation of $\kappa_1 = 0.070$ for critical systems on the basis of the dynamic scaling hypothesis

We deal with time series of signals emitted from complex dynamical systems, i.e., systems consisting of interacting components that evolve with time. In natural time analysis, when the system is in thermodynamic equilibrium, it should produce stationary time series with probabilities p_k independent of χ_k. The situation is drastically different when the system is in non-equilibrium state. When the system approaches the critical state, clusters of the new phase are formed by enhanced fluctuations and their size increases as does the correlation length. But this happens not instantly, because long-range correlations develop gradually leading to the so-called dynamic phase transition (critical transition) (see § 1.5.2). Thus, the time series emitted in such a non-equilibrium process will be non-stationary and p_k, or the corresponding probability density function $p(\chi)$ will no longer be independent of χ.

Using $p(\chi)$, the normalized power spectrum of Eq. (2.31) can be re-written as

$$\Pi(\omega) = \int_0^1 \int_0^1 p(\chi) p(\chi') \cos\left[\omega(\chi - \chi')\right] \, \mathrm{d}\chi \, \mathrm{d}\chi' \tag{8.5}$$

A Taylor expansion of Eq. (8.5) around $\omega \to 0$ leads to the value

$$\kappa_1 = \frac{1}{2} \int_0^1 \int_0^1 p(\chi) p(\chi') \left(\chi - \chi'\right)^2 \, \mathrm{d}\chi \, \mathrm{d}\chi' \tag{8.6}$$

Since $p(\chi)$ is the normalized energy released at χ, for a dynamical system at criticality, it also characterizes the way energy is released during the evolution of the dynamic transition. Energy release may be caused by some existing external field coupled with the newly forming phase. The interaction energy *density* may comprise several terms the most significant of which is usually expected to be of the dipole type; for example the interaction Hamiltonian *density* $h_{\mathrm{int}} = -\mathbf{E} \cdot \mathbf{p}$ ($h_{\mathrm{int}} = -\mathbf{B} \cdot \mathbf{m}$) in the case of an electric $\mathbf{E}$ (magnetic $\mathbf{B}$) external field, where $\mathbf{p}$ ($\mathbf{m}$) stands for the electric (magnetic) dipole moment *density* of the new phase. This interaction energy is proportional to the linear dimension of the newly forming phase (the system volume is kept constant) and hence it is proportional to the correlation length ξ (this will be proven below). According to the *dynamic scaling hypothesis*

(see Refs. [11, 73] and references therein), already explained in § 1.5.3, the time-dependent correlation length ξ at dynamic phase transitions scales as $\xi \propto t^{\frac{1}{z}}$, where z is the so-called dynamic critical exponent. The time t is usually measured in Monte Carlo steps, i.e., using the internal clock of the system. Assuming that the dynamic scaling hypothesis should also hold for $p(\chi)$ at *criticality*, we expect [81]:

$$p(\chi) = N_c \chi^{\frac{1}{\zeta}} \tag{8.7}$$

where ζ is another dynamic exponent (not to be confused with the mean energy ζ of Section 8.3), and N_c a normalization factor to make $\int_0^1 p(\chi)\, \mathrm{d}\chi = 1$. In fact, Eq. (8.7) is plausible from the definition of p_k, i.e., it represents the normalized energy emitted during the k-th event and the energy at criticality has a power law distribution. By inserting Eq. (8.7) into Eq. (8.6), we obtain:

$$\kappa_1 = \frac{1+\zeta}{1+3\zeta} - \left(\frac{1+\zeta}{1+2\zeta}\right)^2 \tag{8.8}$$

Substituting the value of ζ by the dynamic critical exponent z for various universality classes of critical systems [58], we can obtain the values of κ_1 depicted in Fig. 8.14. Notice that for most universality classes, z varies in a region from $z = 2$ to $z = 2.4$ and thus (see Fig. 8.14) the value of κ_1 obtained by Eq. (8.8) are in the range 0.068 to 0.071. Especially for the two-dimensional (2D) Ising model, which is qualitatively similar to the process of SES emission (see § 8.4.1), one has $z = 2.165$ (see Ref. [42]) leading through Eq. (8.8) to $\kappa_1 = 0.0697 \approx 0.070$. These results seem to justify the substitution of ζ by z, strongly suggesting that they are the same dynamic exponent. This is not unreasonable since, in reality, the Monte Carlo steps used in the computation of z actually correspond to natural time steps.

Explanation of the statement that the interaction energy is proportional to the linear dimension of the newly formed phase. Following § 1.5.3, in the non-equilibrium scaling state, the equal-time correlation function $C(r,t)$ (see Eq. (1.37)) of an order parameter field

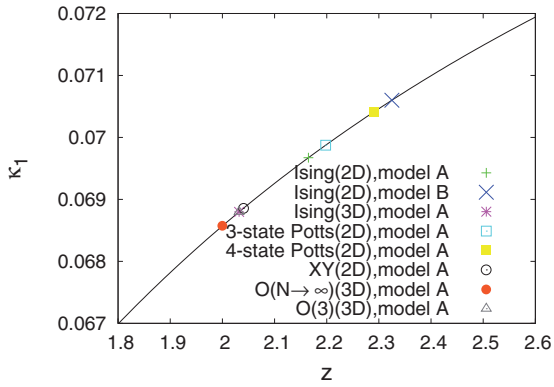

Fig. 8.14 The values of κ_1 as a function of dynamic critical exponent. Various dynamical universality classes are depicted according to their dynamic critical exponent value (see tables IV, VII, IX, XI of Ref. [58]). Models A and B correspond to non-conserved or conserved order parameter dynamics as defined by Hohenberg and Halperin [40]. Taken from Ref. [81]. Note that the value $\kappa_1 = 0.070$ corresponds to $z \approx 2.2$.

$\phi(\mathbf{x},t)$ in the space of D-dimension has the form [12] given by Eq. (1.38) that contains the usual critical exponent η.

It was stated above that the most significant part of the energy release is expected to be of the dipole type, caused by the interaction Hamiltonian $H_{\text{int}} = -\mathbf{E}\cdot\mathbf{P}(= \int_V h_{\text{int}}\,\mathrm{d}\mathbf{x})$, and that this interaction energy is proportional to the linear dimension of the newly forming phase. This statement, following a suggestion of Professor Hiroshi Ezawa, can be shown as follows. The dipole moment $\mathbf{P}$ is given by the integral of its density $\mathbf{p}$

$$\mathbf{P} = \int_V \mathbf{p}(\mathbf{x},t)\,\mathrm{d}\mathbf{x}. \tag{8.9}$$

Assuming $\mathbf{p}(\mathbf{x},t)$ fluctuating under a given electric field $\mathbf{E}$, one focuses on the magnitude P, considering that

$$P^2 = \int \mathrm{d}\mathbf{x} \int \mathrm{d}\mathbf{x}' \mathbf{p}(\mathbf{x},t)\cdot\mathbf{p}(\mathbf{x}',t),$$

which, on average, is related to the correlation function (see Eq. (1.37)) by

$$\begin{aligned}\left\langle P^2 \right\rangle &= \int \mathrm{d}\mathbf{x} \int \mathrm{d}\mathbf{x}' \left\langle \mathbf{p}(\mathbf{x},t)\cdot\mathbf{p}(\mathbf{x}',t)\right\rangle \\ &= \int \mathrm{d}\mathbf{x} \int \mathrm{d}\mathbf{r} \left\langle \mathbf{p}(\mathbf{x},t)\cdot\mathbf{p}(\mathbf{x}+\mathbf{r},t)\right\rangle \\ &= D\int_V \mathrm{d}\mathbf{x} \int_0^R S_D\, r^{D-1} C(r,t)\,\mathrm{d}r,\end{aligned} \tag{8.10}$$

where V is D-dimensional and S_D is the surface area of the unit sphere in D dimensions, and $C(r,t)$ is given by Eq. (1.38), so that

$$\begin{aligned}\left\langle P^2 \right\rangle &= DVS_D \int_0^R \frac{c}{r^{\eta-1}} f\left(\frac{r}{\xi(t)}\right)\mathrm{d}r \\ &= DVS_D \frac{c}{\xi(t)^{\eta-2}} \int_0^\infty \frac{c}{s^{\eta-1}} f(s)\,\mathrm{d}s \propto \frac{1}{\xi(t)^{\eta-2}} = \xi(t)^{2-\eta},\end{aligned} \tag{8.11}$$

irrespective of the dimensionality D of V, where we have changed the variable of integration from r to $s = r/\xi(t)$ assuming $V \to \infty$. Since $\eta \approx 0$ irrespective of the dimensionality D of V (e.g., see Ref. [8]), Eq. (8.11) leads to

$$\sqrt{\left\langle P^2 \right\rangle} \propto \xi(t), \tag{8.12}$$

which gives a linear growth of $P = \sqrt{\left\langle P^2 \right\rangle}$ with $\xi(t)$.

8.4.1 Natural time analysis of the 2D Ising model quenched close to, but below, T_c. The qualitative similarity to the original SES generation model

Here we treat the case of quenching a ferromagnetic Ising system from a high temperature state to a temperature close to (but below) the critical temperature. This case is studied

here since it is qualitatively similar to the pressure stimulated currents (PSC) generation mechanism of SES [78] (see § 1.6.2) in the following sense. In the focal region of a future earthquake, which contains ionic materials, the stress gradually changes before failure. In ionic solids containing aliovalent impurities, extrinsic defects are formed due to charge compensation, which are attracted by nearby aliovalent impurities, thus forming electric dipoles that can change their orientation in space through a defect migration. Stress variations may decrease the relaxation time of these dipoles and when the pressure, or the stress in general, reaches a critical value a *cooperative* orientation of these electric dipoles occurs, which results in the emission of a transient electric signal, which constitutes the SES. The amount of energy released during this relaxation is proportional to the electric dipole moment. This phenomenon may be considered as qualitatively similar to a rapid quench of a ferromagnetic Ising system from a high temperature state (corresponding to the initial random orientations of the magnetic dipoles) to a temperature close and below the critical temperature T_c. Of course, in the case of PSC and hence for the SES, it is not the temperature that changes, but it is the pressure. Pressure variations modify the coupling between the dipoles so that effectively the critical state is reached.

The calculations have been carried out as follows. A 2D Ising system (with Hamiltonian $H = -J\sum_{\langle ij \rangle} s_i s_j$, where $s_i = \pm 1$ and J stands for the coupling constant between the nearest neighbors s_i and s_j) in a square lattice of linear size L (with periodic boundary conditions) was prepared in a high-temperature state and then instantaneously quenched to a temperature (just) below T_c. The evolution of the magnetization per spin $M_k = \sum s_i / L^2$ was simulated by the standard Metropolis algorithm and studied as a function of the number k of Monte Carlo steps (MCS). The latter was set to zero when the system is quenched at a temperature close but below T_c, and increased by 1 after each Monte Carlo step, i.e., after all the spins of the system have been renewed following the standard Metropolis algorithm. For the purpose of the present simulation, k runs from $k = 1$ to 10^4 MCS. Figure 8.15(a) depicts the ensemble average $\langle |M_k| \rangle$ of $|M_k|$ obtained from 10^3 replicas for various sizes $L = 100$, 200, 400 and 1,000. It is observed in the figure that, due to the well-known phenomenon of critical slowing down [48], systems of larger linear size need larger number of MCS to finally reach the equilibrium magnetization. We now present in Fig. 8.15(b) a log-log plot of the values shown in Fig. 8.15(a). This reveals that, practically independent of L, the dynamics of $\langle |M_k| \rangle$ is a power law: $\langle |M_k| \rangle \propto k^{1/z}$ with the dynamic exponent z very close to [42] $z = 2.165$ (see the thick cyan straight line in Fig. 8.15(b)).

This dynamic model was then analyzed in natural time by setting $Q_k = |M_k|$. Figure 8.15(c), which depicts the results for κ_1 as a function of the number k of Monte Carlo steps that followed the instantaneous quench, clearly shows that $\kappa_1 \approx 0.070$.

This result coincides with the one obtained above (i.e., $\kappa_1 = 0.0697$) in § 8.4, when substituting in Eq. (8.8) ζ by the aforementioned value $z = 2.165$.

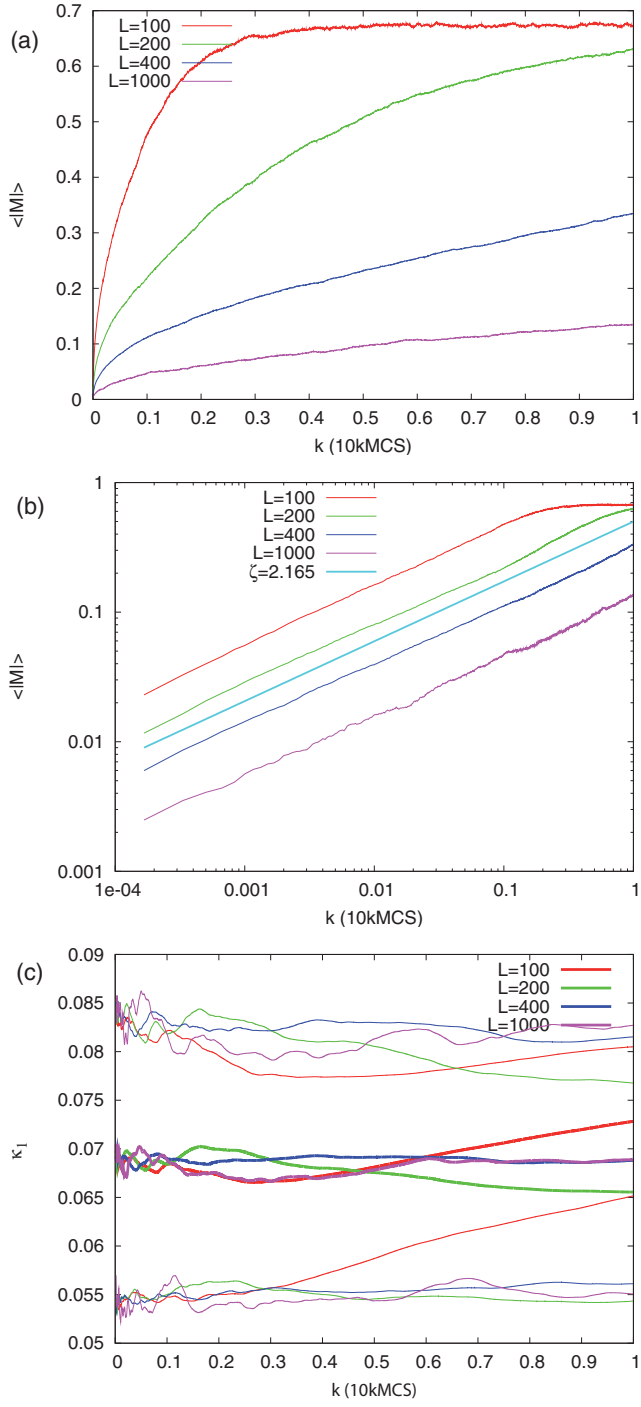

Fig. 8.15 (a), (b) Evolution of $\langle |M_k| \rangle$ as a function of the number k of MCS, after an abrupt quench close but below T_c, up to $k = 10^4$. The thick line in (b) corresponds to $z = 2.165$ (see Ref. [42]) and is drawn as a guide to the eye. (c) depicts the evolution of κ_1 as a function of k when $|M_k|$ is analyzed in natural time. The average value of κ_1 is drawn with the thick lines, whereas the thinner lines enclose the one standard deviation $(\mu \pm \sigma)$ confidence interval. The results were found by 10^3 runs of the model for various L. Taken from Ref. [81].

8.4.2 The original Bak–Tang–Wiesenfeld sandpile SOC model and its fully deterministic version. Natural time analysis

Here, we come back to the original archetypal "sandpile" automaton described in Ref. [6] (see also Section 8.1), hereafter called the Bak–Tang–Wiesenfeld (BTW) model. Let us consider the D-dimensional BTW model on a hypercubic lattice of linear size L in which integer variables $z_i \geq 0$ represent units of sand. We perturb the system by adding a unit of sand at a *randomly chosen* site $z_i \to z_i + 1$. If the corresponding z_i exceeds the critical value $2D$, the site is called unstable; an unstable site relaxes (topples): its z_i value is decreased by $2D$, and the amount of units of sand of its $2D$ nearest neighbors (nn) is increased by one:

$$z_i \to z_i - 2D \tag{8.13}$$

$$z_{\mathrm{nn}} \to z_{\mathrm{nn}} + 1 \tag{8.14}$$

Thus, the neighboring sites may be activated and an avalanche of relaxations may proceed. This avalanche stops when all sites are stable again. A relaxation event is characterized by its size s (total number of topplings), area a (number of distinct toppled sites), duration t (number of parallel update steps until stable configuration is reached), and its radius r (e.g., the maximal distance between the original and a toppled site). According to the basic hypothesis of Bak et al. [6], in the SOC state the probability distributions of values $x = s, a, t, r$ exhibit power law behavior

$$P_x(\mathrm{x}) \propto \mathrm{x}^{-\tau_x} \tag{8.15}$$

with $x \in \{s, a, t, r\}$. According to Ref. [47], Eq. (8.15) might *not* be in general true for complete avalanches but it does hold for waves of topplings. Specifically, waves represent relaxation processes in which any site topples at most once and hence do not contain multiple toppling events in the origin of the avalanche (note that the latter, for $D \geq 4$, are so rare that they can be neglected). Ktitarev et al. [47] proved analytically that the upper critical dimension of the BTW model is $D_u = 4$, showing that previously observed deviations from mean field behavior at $D = 4$ are due to logarithmic corrections. For this case, $D = 4$, the scaling behavior of waves *and* avalanches is characterized by the same exponents and scaling functions.

In order to proceed to numerical simulations, we study a *fully* deterministic version of the BTW sandpile model, where the random site seeding is replaced by regular seeding at the central site of the hypercubic lattice, suggested by Wiesenfeld et al. [84]. They showed that despite this strict determinism, the system for $D = 2$ evolves into a SOC state. The natural time analysis (with initial condition $z_i = 0$) of the time series of avalanches lead to κ_1 values plotted in Fig. 8.16 for $D = 2$ to $D = 7$. Focusing on the aforementioned upper critical dimension (hence corresponding to the mean field case) $D = 4$, we see that the κ_1 value fluctuates close to 0.070.

The κ_1 values for various D plotted in Fig. 8.16 fluctuate around the value obtained from Eq. (8.8) for $\zeta = D/2$, i.e., 0.056 for $D = 2$, 0.064 for $D = 3$, 0.069 for $D = 4$, 0.071 for $D = 5$, 0.073 for $D = 6$ and 0.075 for $D = 7$. This result can be understood on the following grounds.

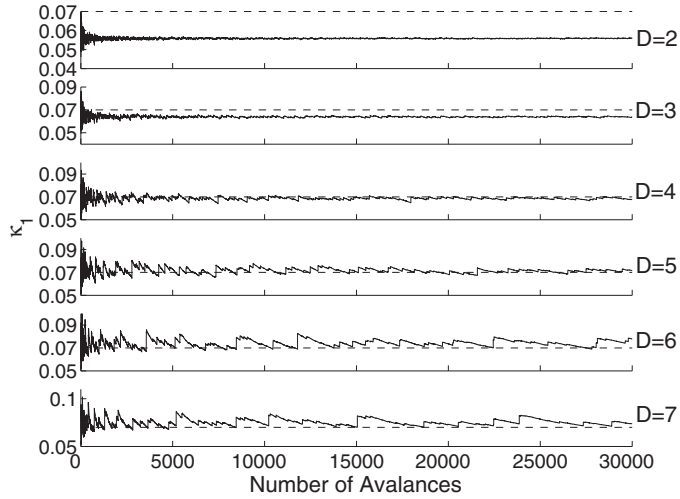

Fig. 8.16 The evolution of κ_1 values versus the number of consecutive avalanches for various D values, i.e., for $D = 2$ to $D = 7$, for the centrally fed sandpile. The initial condition is $z_i = 0$. For the sake of comparison, the broken horizontal line shows the value of $\kappa_1 = 0.070$. Taken from Ref. [81].

Since an avalanche occurs every $2D$ seeds are fed into the central site, the number of avalanches is equal to the number of seeds n fed divided by $2D$. Natural time increases by $1/N$ when an avalanche occurs, thus we have

$$\chi_k = \frac{k}{N}, \;\; k = \left[\frac{n}{2D}\right]. \tag{8.16}$$

where the brackets $[\cdot]$ denote the integer part. The local conservation of the units of sand (i.e., sand particles can move only to nearest neighbors sites) expressed in Eqs. (8.13) and (8.14), leads to the fact that the expected number of toppling G_{ij} at site j, upon adding a particle at site i is characterized by [27]

$$G_{ij} \propto r_{ij}^{2-D}, \tag{8.17}$$

where r_{ij} is the distance between the sites i and j. Since we deal with a centrally fed sandpile, the total expected number of topplings $\langle s \rangle$ is found by integrating Eq. (8.17) in the hypersphere of radius l of the sandpile:

$$\langle s \rangle \propto \int_0^l G_{0j} S_D r_{0j}^{D-1} \, \mathrm{d}r_{0j} \propto \int_0^l r_{0j} \, \mathrm{d}r_{0j} \propto l^2. \tag{8.18}$$

With regard to l, recent mathematical studies [31] show that the linear dimension of the formed sandpile grows as

$$l \propto n^{1/D} \tag{8.19}$$

Inserting Eqs. (8.16) and (8.19) into Eq. (8.18), we obtain $\langle s \rangle \propto \chi^{2/D}$ which reflects (cf. Eq. (8.7)) that $\zeta = D/2$.

Notice that for the upper critical dimension, we have $D = D_u = 4$, and hence $\zeta = 2$ (which is equal to the *mean field dynamic exponent* $z = 2$, e.g. see Ref. [47]) which, in view of Eq. (8.8), leads to $\kappa_1 = 0.0686 (\approx 0.070)$.

The fulfillment of the condition $\kappa_1 = 0.070$ could be alternatively seen as follows when considering some points discussed in Ref. [17]: The relaxation of a site can induce a number of other sites to relax in turn if, because of the particles received, they exceed the threshold. From the moment a site topples, the addition of particles stops until all sites have relaxed ($z_i < 2D$ for all i, see Eq. (8.13)). This condition assures that the driving force is *'slow'* being the driving time exceedingly longer than the characteristic time of toppling instances. The sequence of toppling events during this interval constitutes an avalanche. For conservative models, the number of transferred particles equals the number of particles lost by the relaxing site and dissipation occurs only at boundary, from which particles can escape the system. Under these conditions the system reaches a stationary state characterized by a sequence of avalanches. Since the SOC algorithm is implemented basically as a cellular automaton, the *cluster growth is intrinsically of diffusive nature*.

It is this *diffusive* nature of the cluster growth, which seems to lie behind the aforementioned result $\kappa_1 = 0.070$ in SOC models.

8.4.3 Natural time analysis of the mean field case

As mentioned above in Section 8.4 for most universality classes, z varies in a region from $z = 2$ to $z = 2.4$ and thus (see Fig. 8.14) the values of κ_1 obtained by Eq. (8.8) are in the range 0.068 to 0.071. Moreover, in the mean field case, e.g. of the *growing* centrally fed sandpile in § 8.4.2, we have

$$\zeta = 2. \tag{8.20}$$

By inserting Eq. (8.20) into Eq. (8.7), we get

$$p(\chi) = \frac{3}{2}\sqrt{\chi} \tag{8.21}$$

so that $\int_0^1 p(\chi)\, \mathrm{d}\chi = 1$. Upon using Eq. (8.21) for the estimation of the variance κ_1 of natural time (see Eq. (2.37))

$$\kappa_1 = \int_0^1 \chi^2 p(\chi)\, \mathrm{d}\chi - \left[\int_0^1 \chi p(\chi)\, \mathrm{d}\chi\right]^2, \tag{8.22}$$

we find and the corresponding κ_1 value is $\kappa_1 = 0.0686$. This value almost coincides with the value $\kappa_1 \approx 0.070$ found (see Chapter 7) from the natural time analysis of seismicity before large EQs.

The stability of the result $\kappa_1 \approx 0.070$ *if a single realization of the process is available.* The results of this investigation, depicted in Fig. 8.17, show the following:

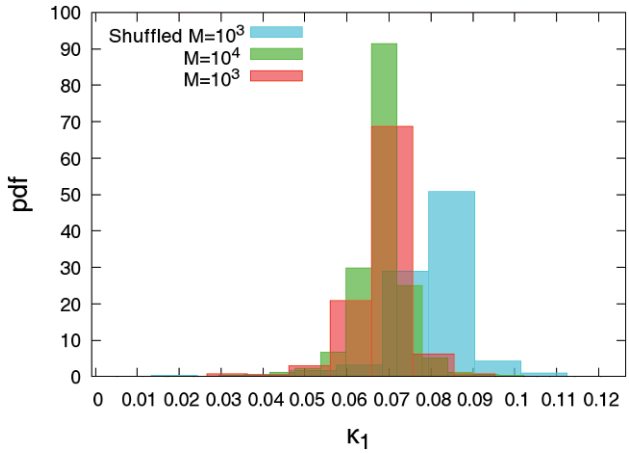

Fig. 8.17 The probability distribution of κ_1 obtained after randomly selecting $M = 10^3$ (red) or $M = 10^4$(green) subseries from a single realization of the process described by Eq. (8.21) using exponentially distributed Q_k (see the text). Both distributions are peaked close to $\kappa_1 = 0.070$. Once the events of the original realization are shuffled randomly and then $M = 10^3$ subseries are analyzed, the peak of the new distribution, shown in cyan, is displaced to the right.

Even when using a single realization of the process described by Eq. (8.21) with Q_k exponentially distributed, i.e., $Q_k = r_k\sqrt{k}$ where r_k are exponential p.i.i.d. random variables, and select random subseries of the process to be analyzed in natural time, the pdf deduced for κ_1 maximizes at $\kappa_1 \approx 0.070$.

This is reminiscent of the *updated* procedure used in § 7.1.2. This so, because in that procedure we considered the time series of seismicity that occurs after the initiation of the SES activity in the area candidate to suffer a mainshock and then used the subseries corresponding to the seismicity in all possible subareas of the candidate area to construct the pdf of the resulting κ_1 values. It was then found that this pdf exhibits a maximum at $\kappa_1 \approx 0.070$ when approaching the occurrence time of the mainshock.

8.5 Natural time analysis of time series of avalanches observed in laboratory experiments

8.5.1 Time series of avalanches observed in ricepiles

Here, we consider the well-controlled experiment on three-dimensional ricepiles by Aegerter et al. [2, 1]. Since a genuine understanding of the nature of SOC can be gained only when the *approach* to the critical state is understood, Aegerter et al. studied the evolution of

a three-dimensional pile of rice starting well away from the critical state and getting progressively closer. They found [1] that their experimental results are satisfactorily described by well-founded concepts proposed [60] in the context of extremal dynamics. In the latter context, Paczuski et al. [60] have derived an equation (predicting power law behavior), which they call the gap equation, describing the approach of the system to the critical state. Aegerter et al. [2] directly studied a measure of this gap given by the maximal local slope of the ricepile and hence could test various scaling relations of extremal dynamics. Furthermore, Aegerter et al. studied the evolution of avalanche sizes, as well as that of the avalanche distributions, which can be used as further tests of extremal dynamics aspects. Here we solely focus on the way the size ΔV of avalanches grow with time in the transient regime, which was measured directly.

Figure 8.18(a) depicts the time evolution of ΔV obtained in one experiment of Ref. [2]. Upon analyzing these data in natural time when assuming $Q_k = \Delta V_k$, we find the results shown in Fig. 8.18(b).

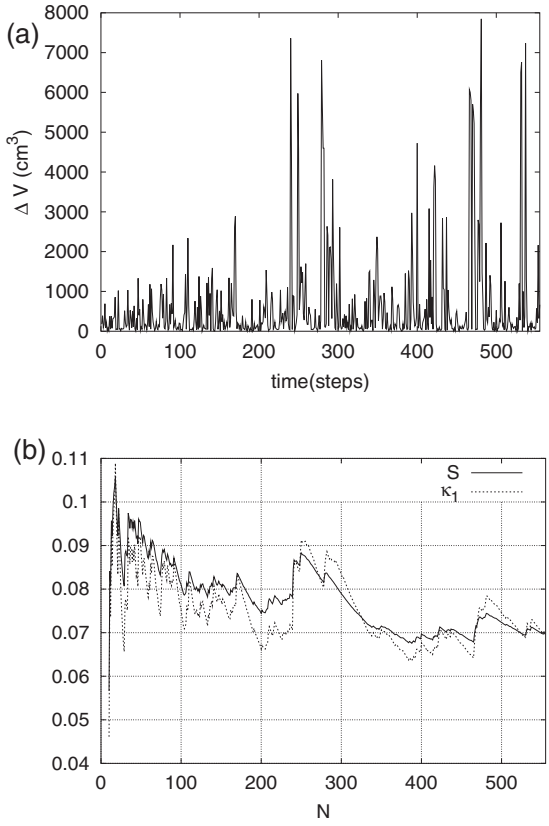

Fig. 8.18 (a): The evolution of the avalanche sizes, in the transient regime, for one of the experiments of Ref. [2] on ricepiles. (b): The results of the variance κ_1 (dotted) and the entropy S (solid) as they evolve event by event, when the data of (a) are analyzed in natural time. Taken from Ref. [70].

A careful inspection of these results in ricepiles reveals that actually at later times ($N \geq 350$) the κ_1 value scatters in the region around 0.070(10) (as well as that $S \approx 0.070(10) < S_u$).

We clarify that upon shuffling the data, which reflects that the values are put into random order and hence all correlations (memory) are destroyed [80] (see also § 2.5.2.1), we find that, for $N = 550$, $\text{Prob}[\kappa_1 \leq 0.070] < 2\%$ (and $\text{Prob}[S \leq 0.070] < 0.1\%$). This leads to the following conclusion:

The *sequential order* of the avalanches captured by the natural time analysis is of prominent importance [70] for establishing the SOC state and constitutes the basis for the observation of the result $\kappa_1 \approx 0.070$.

8.5.2 Time series of magnetic flux avalanches observed in high T_c superconductors. A generalized stochastic directed SOC model

The archetypal example of SOC is, as mentioned (Section 8.1 and § 8.2.2), the growing of a sandpile [6, 7]. Furthermore, the critical state in superconductors has been proposed (e.g. see Ref. [87]) to be a SOC system. The strong analogy between these two systems, i.e., sandpiles and superconductors, as first pointed out by de Gennes (see p.83 of Ref. [34]), could be in principle understood as follows.

When a type II superconductor is put in a slowly ramped external field, magnetic vortices start to penetrate the sample from its edges. These vortices get pinned by crystallographic defects (e.g., dislocations [78]), leading to the build-up of a flux gradient which is only marginally stable in a similar fashion as is the slope in a slowly growing sandpile. Hence, it can happen that small changes in the applied field can result in large rearrangements of flux in the sample, known as flux avalanches [15, 4, 83].

We now proceed to the natural time analysis of the time series of the magnetic flux avalanches measured in a thin film of $YBa_2Cu_3O_{7-x}$. These measurements have been made by Aegerter et al. [3]. They studied the local changes in the magnetic flux over the whole central area of a sample via a highly sensitive magneto-optic setup, which allows that flux changes corresponding to $2.5\Phi_0$ can be resolved where $\Phi_0 = h/2e$ is the magnetic flux quantum (the flux of a single vortex). The pinning sites in the sample were uniformly distributed and consisted mostly of screw dislocations acting as point pins. For cuprate high T_c superconductors such as $YBa_2Cu_3O_{7-x}$ the coherence lengths are in the order of tens of Å, and thus atomic-scale structural inhomogeneities such as point defects and columnar defects can play an important role in flux-line pinning. (In these superconductors, Su et al. [77] found that Schottky defects formation energy increases almost linearly with $B\Omega$, where B is the isothermal bulk modulus and Ω the mean volume per atom, in striking agreement with an early model (termed the $cB\Omega$ model) proposed [79, 78] by one of the present authors.)

The data of Aegerter et al. [3] come from experimental runs consisting of 140 time steps. The size and shape of the avalanches was determined from the difference $\Delta B_z(x,y)$ of two consecutive images (50 μT increase between images), where $B_z(x,y)$ denotes the flux density at the surface of the sample measured. From these differences, the average increase in the applied magnetic field due to the stepwise field sweep, was subtracted in order to solely study the avalanches. Once the incremental field difference is determined, the size of an avalanche, corresponding to the displaced amount of flux $\Delta\Phi$, is estimated from ΔB_z by integrating over the whole area $\Delta\Phi = \frac{1}{2}\int \Delta B_z(x,y)\,\mathrm{d}x\,\mathrm{d}y$.

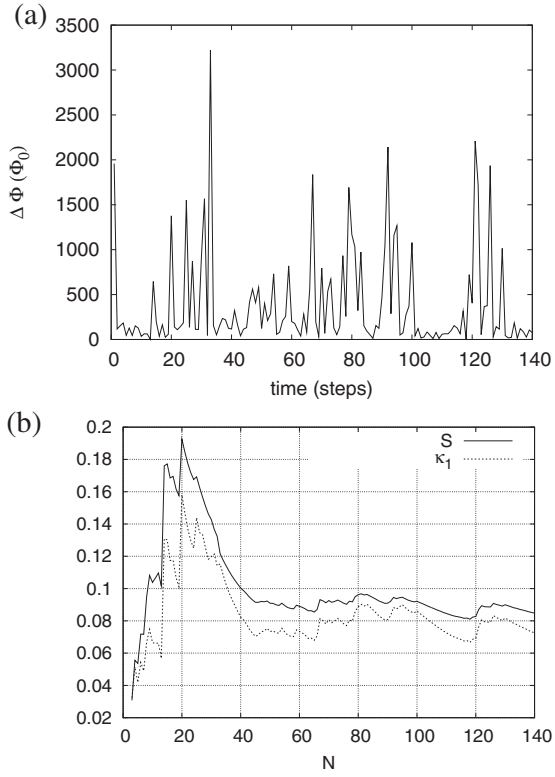

Fig. 8.19 (a): The time evolution of the magnetic flux in $YBa_2Cu_3O_{7-x}$ inside the sample over the 1st run of fig.2 of Ref. [3]. (b): The results of the variance κ_1 (dotted) and the entropy S (solid) as they evolve event by event, when the data of (a) are analyzed in the natural time-domain. Taken from Ref. [70].

The time series of the avalanche behavior in a typical experiment of Aegerter et al. [3] is depicted in Fig. 8.19(a), which shows that the evolution of the magnetic flux inside the sample is intermittent with occasional large jumps. Figure 8.19(b) depicts the results obtained [70] when the data of Fig. 8.19(a) are analyzed in natural time by assuming $Q_k = \Delta\Phi_k$.

An inspection of the latter figure shows that for $N = 140$ the κ_1 value is close to 0.070(5) (as well as that the S value is around 0.085, i.e., smaller than S_u).

The results obtained above have been compared [70] with those deduced from the natural time analysis of the numerical results from a generalized stochastic SOC model suggested by Carbone and Stanley [17]. It consists of a family of stochastic directed clusters generated by fractional Brownian paths with different correlation properties. Carbone and Stanley showed that the cluster area, length and duration exhibit the characteristic scaling behavior of SOC clusters. This model is considered [17] to be a generalized stochastic model, including the Dhar-Ramaswamy [28] directed sandpile model (which can be described assuming that the system is driven by particles added at the top layer $i = 0$ and removed from the bottom layer $i = L$) and the stochastic models as particular cases.

Carbone and Stanley [17] consider a generalized Brownian walk $y(i)$ defined by $y(i) \equiv \sum_{k=0}^{i-1} \xi_k$, where the steps ξ_k are taken from a discrete fGn (see § 1.5.1.1). The mean square displacement of $y(i)$ scales with Δi as $\langle y(i)^2 \rangle \propto (\Delta i)^{2H}$, where H is the Hurst exponent ($0 < H < 1$). The moving average function $\tilde{y}_n(i)$ is

$$\tilde{y}_n(i) \equiv \frac{1}{n} \sum_{k=0}^{n-1} y(i-k), \tag{8.23}$$

which is a linear operator whose output is still a generalized Brownian motion, but now with the high-frequency components of the signals averaged out [16] according to the window amplitude n. In order to characterize the clusters $\mathscr{C}$ corresponding to the regions bounded by $y(i)$ and $\tilde{y}_n(i)$ in terms of the characteristic exponents of SOC systems, they define – for each cluster – the cluster area s_j

$$s_j \equiv \sum_{i=i_c(j)}^{i_c(j+1)} |y(i) - \tilde{y}_n(i)| \Delta i, \tag{8.24}$$

where the index j refers to each cluster. The symbols $i_c(j)$ and $i_c(j+1)$ stand [17] for the values of the index i corresponding to two subsequent intersections of the "lines" defined by $\tilde{y}_n(i)$ and $y(i)$, and Δi is the elementary time interval corresponding to each step of the random walker. Then, the pdf $P(s)$ scales [17] as $P(s) \propto s^{-\tau}$ with $\tau = 2/(1+H)$. Considering that the exponent of the avalanche distribution reported from the data analysis of Aegerter et al. [3] is around $\tau = 1.3$, we find that it corresponds to $H \approx 0.5$. Thus, in Fig. 8.20, we plot $P(s)$ versus s calculated for various n values for $H = 0.5$.

We now turn to the comparison of the results of this model with the aforementioned experimental results in $YBa_2Cu_3O_{7-x}$ films. Taking into account that the maximum avalanche size s_{max} detected by Aegerter et al. [3] is of the order of 10^4, an inspection of Fig. 8.20 leads to $n \approx 200$. In Fig. 8.21, we plot with solid lines the pdfs of κ_1 and S that have been obtained from the model of Ref. [17] for $H = 0.5$, $n = 200$ and $N = 140$. An inspection of this figure shows that:

The maxima of the pdfs of κ_1 and S lie around $\kappa_1 = 0.070(10)$ and $S = 0.080(10)$, respectively. These are comparable with the corresponding κ_1 and S values obtained from the natural time analysis of the experimental data depicted in Fig. 8.19(b) (for $N = 140$).

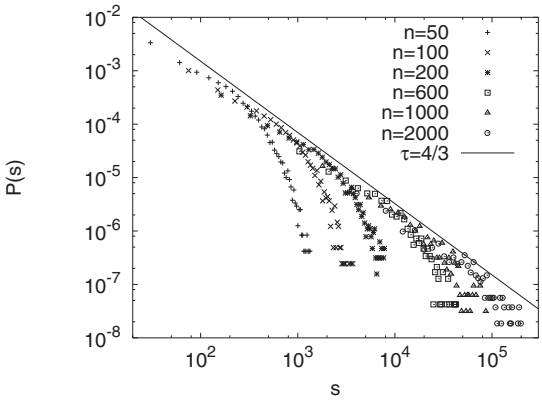

Fig. 8.20 The pdf $P(s)$ versus the cluster area s of the $\mathscr{C}$ clusters of Ref. [17], for $H = 0.5$ for various values of $n = 50$, 100, 200, 600, 1,000 and 2,000. The line $P(s) \propto s^{-\tau}$ with $\tau = 4/3$, as analytically found in Ref. [17] to describe $P(s)$, is also drawn as a guide to the eye. Taken from Ref. [70].

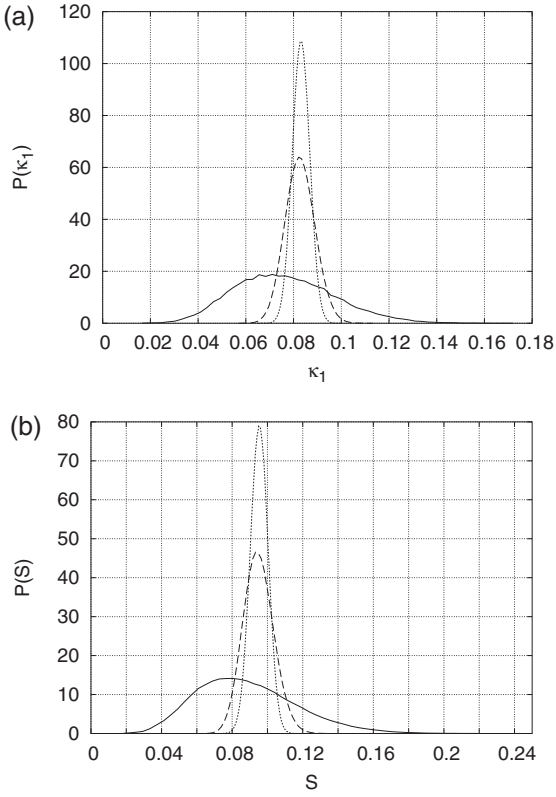

Fig. 8.21 The pdfs of κ_1 and S obtained from a Monte Carlo simulation for the generalized stochastic model of Ref. [17] for $H = 0.5$, $n = 200$ and $N = 140$. The dotted and dashed pdfs correspond to two different *non*-critical cases(see the text). Taken from Ref. [70].

For the sake of comparison, in Fig. 8.21, we also plot the corresponding pdfs for two *non-critical* cases associated with a "uniform" distribution (see § 2.1.3) i.e., (i) when Q_k are uniformly distributed in the range (0,1) (dotted) and (ii) when Q_k are exponentially distributed (broken) which corresponds to a dichotomous Markovian process (see Sec-

tion 4.1), e.g, the case of the observed [25] RTS signals in metal-oxide-semiconductor transistors with tunneling oxide. The maxima of the latter two cases lie at $\kappa_1 \approx \kappa_u$ and $S \approx S_u$, which markedly differ from those deduced for $YBa_2Cu_3O_{7-x}$ in Fig. 8.19(b) (for $N = 140$).

By summarizing, the measurements of the penetration of magnetic flux into a thin film of $YBa_2Cu_3O_{7-x}$ have been analyzed in natural time. This analysis leads to a value of the variance $\kappa_1 = \langle \chi^2 \rangle - \langle \chi \rangle^2$ equal to $\kappa_1 \approx 0.070$. The same κ_1 value is found from the natural time analysis of a generalized stochastic SOC model proposed by Carbone and Stanley [17].

Acknowledgments We express our sincere thanks Professor Rinke J. Wijngaarden, for sending us the $YBa_2Cu_3O_{7-x}$ and ricepile data discussed in § 8.5.2 and § 8.5.1, respectively.

References

1. Aegerter, C.M., Gunther, R., Wijngaarden, R.J.: Avalanche dynamics, surface roughening, and self-organized criticality: Experiments on a three-dimensional pile of rice. Phys. Rev. E **67**, 051306 (2003)
2. Aegerter, C.M., Lorincz, K.A., Welling, M.S., Wijngaarden, R.J.: Extremal dynamics and the approach to the critical state: Experiments on a three dimensional pile of rice. Phys. Rev. Lett. **92**, 058702 (2004)
3. Aegerter, C.M., Welling, M.S., Wijngaarden, R.J.: Self-organized criticality in the bean state in $YBa_2Cu_3O_{7-x}$ thin films. Europhys. Lett. **65**, 753–759 (2004)
4. Altshuler, E., Johansen, T.H.: Colloquium: Experiments in vortex avalanches. Rev. Mod. Phys. **76**, 471–487 (2004)
5. Bach, M., Wissel, F., Drossel, B.: Olami–Feder–Christensen model with quenched disorder. Phys. Rev. E **77**(6), 067101 (2008)
6. Bak, P., Tang, C., Wiesenfeld, K.: Self-organized criticality: An explanation of the 1/f noise. Phys. Rev. Lett. **59**(4), 381–384 (1987)
7. Bak, P., Tang, C., Wiesenfeld, K.: Self-organized criticality. Phys. Rev. A **38**, 364–374 (1988)
8. Binney, J.J., Dowrick, N.J., Fisher, A.J., Newman, M.E.J.: The Theory of Critical Phenomena – An Introduction to the Renormalization Group. Oxford University Press, UK (1992)
9. Bonachela, J.A., Mũnoz, M.A.: Self-organization without conservation: true or just apparent scale-invariance? J. Stat. Mech. P09009 (2009)
10. Boulter, C.J., Miller, G.: Nonuniversality and scaling breakdown in a nonconservative earthquake model. Phys. Rev. E **68**, 056108 (2003)
11. Bray, A.J.: Theory of phase-ordering kinetics. Adv. Phys. **43**, 357–459 (1994)
12. Bray, A.J., Briant, A.J., Jervis, D.K.: Breakdown of scaling in the nonequilibrium critical dynamics of the two-dimensional *XY* model. Phys. Rev. Lett. **84**, 1503–1506 (2000)
13. Bröker, H.M., Grassberger, P.: Random neighbor theory of the Olami–Feder–Christensen earthquake model. Phys. Rev. E **56**, 3944–3952 (1997)
14. Burridge, R., Knopoff, L.: Model and theoretical seismicity. Bull. Seismol. Soc. Am. **57**, 341–371 (1967)
15. Campbell, A.M., Evetts, J.E.: Flux vortices and transport currents in type II superconductors. Adv. Phys. **50**, 1249–1449 (2001)
16. Carbone, A., Castelli, G., Stanley, H.E.: Analysis of clusters formed by the moving average of a long-range correlated time series. Phys. Rev. E **69**, 026105 (2004)

17. Carbone, A., Stanley, H.E.: Directed self-organized critical patterns emerging from fractional Brownian paths. Physica A **340**, 544–551 (2004)
18. Carlson, J.M., Langer, J.S.: Properties of earthquakes generated by fault dynamics. Phys. Rev. Lett. **62**, 2632–2635 (1989)
19. Carlson, J.M., Langer, J.S., Shaw, B.E.: Dynamics of earthquake faults. Rev. Mod. Phys. **66**, 657–670 (1994)
20. Caruso, F., Pluchino, A., Latora, V., Vinciguerra, S., Rapisarda, A.: Analysis of self-organized criticality in the Olami–Feder–Christensen model and in real earthquakes. Phys. Rev. E **75**, 055101 (2007)
21. de Carvalho, J.X., Prado, C.P.C.: Self-organized criticality in the Olami–Feder–Christensen model. Phys. Rev. Lett. **84**, 4006–4009 (2000)
22. de Carvalho, J.X., Prado, C.P.C.: Dealing with transients in models with self-organized criticality. Physica A **321**, 519–528 (2003)
23. Ceva, H.: Influence of defects in a coupled map lattice modeling earthquakes. Phys. Rev. E **52**, 154–158 (1995)
24. Chabanol, M.L., Hakim, V.: Analysis of a dissipative model of self-organized criticality with random neighbors. Phys. Rev. E **56**, R2343–R2346 (1997)
25. Chen, M.J., Lu, M.P.: On-off switching of edge direct tunneling currents in metal-oxide-semiconductor field-effect transistors. Appl. Phys. Lett.. **81**, 3488–3490 (2002)
26. Davidsen, J., Paczuski, M.: $1/f^{\alpha}$ noise from correlations between avalanches in self-organized criticality. Phys. Rev. E **66**, 050101 (2002)
27. Dhar, D.: Theoretical studies of self-organized criticality. Physica A **369**, 29–70 (2006)
28. Dhar, D., Ramaswamy, R.: Exactly solved model of self-organized critical phenomena. Phys. Rev. Lett. **63**, 1659–1662 (1989)
29. Drossel, B.: Complex scaling behavior of nonconserved self-organized critical systems. Phys. Rev. Lett. **89**, 238701 (2002)
30. Fawcett, T.: An introduction to ROC analysis. Pattern Recogn. Lett. **27**, 861–874 (2006)
31. Fey, A., Levine, L., Peres, Y.: Growth rates and explosions in sandpiles. J. Stat. Phys. **138**, 143–159 (2010)
32. Garber, A., Hallerberg, S., Kantz, H.: Predicting extreme avalanches in self-organized critical sandpiles. Phys. Rev. E **80**, 026124 (2009)
33. Garber, A., Kantz, H.: Finite-size effects on the statistics of extreme events in the BTW model. Eur. Phys. J. B **67**, 437–443 (2009)
34. de Gennes, P.G.: Superconductivity of Metals and Alloys. Addison-Wesley, New York (1966)
35. Grassberger, P.: Efficient large-scale simulations of a uniformly driven system. Phys. Rev. E **49**, 2436–2444 (1994)
36. Helmstetter, A., Hergarten, S., Sornette, D.: Properties of foreshocks and aftershocks of the nonconservative self-organized critical Olami–Feder–Christensen model. Phys. Rev. E **70**, 046120 (2004)
37. Helmstetter, A., Sornette, D.: Foreshocks explained by cascades of triggered seismicity. J. Geophys. Res. **108(B10)**, 2457 (2003)
38. Helmstetter, A., Sornette, D., Grasso, J.R.: Mainshocks are aftershocks of conditional foreshocks: How do foreshock statistical properties emerge from aftershock laws. J. Geophys. Res. **108(B1)**, 2046 (2003)
39. Hergarten, S., Neugebauer, H.J.: Foreshocks and aftershocks in the Olami–Feder–Christensen model. Phys. Rev. Lett. **88**, 238501 (2002)
40. Hohenberg, P.C., Halperin, B.I.: Theory of dynamic critical phenomena. Rev. Mod. Phys. **49**, 435–479 (1977)
41. Huang, Y., Saleur, H., Sammis, C., Sornette, D.: Precursors, aftershocks, criticality and self-organized criticality. Europhys. Lett. **41**, 43–48 (1998)
42. Ito, N.: Non-equilibrium relaxation and interface energy of the Ising model. Physica A **196**, 591–614 (1993)
43. Jánosia, I.M., Kertész, J.: Self-organized criticality with and without conservation. Physica A **200**, 179–188 (1993)
44. Jensen, H.J.: Self-organized criticality: emergent complex behavior in physical and biological systems. Cambridge University Press, New York (1998)

45. Keilis-Borok, V.I., Kossobokov, V.G.: Premonitory activation of earthquake flow: algorithm M8. Phys. Earth Planet. Inter. **61**, 73–83 (1990)
46. Keilis-Borok, V.I., Rotwain, I.M.: Diagnosis of time of increased probability of strong earthquakes in different regions of the world: algorithm CN. Phys. Earth Planet. Inter. **61**, 57–72 (1990)
47. Ktitarev, D.V., Lübeck, S., Grassberger, P., B. Priezzhev, V.: Scaling of waves in the Bak–Tang–Wiesenfeld sandpile model. Phys. Rev. E **61**, 81–92 (2000)
48. Landau, D.P., Binder, K.: A Guide to Monte Carlo Simulations in Statistical Physics. Cambridge Univ. Press, New York (2005)
49. Lee, M.J.: Pseudo-random-number generators and the square site percolation threshold. Phys. Rev. E **78**, 031131 (2008)
50. Lippiello, E., de Arcangelis, L., Godano, C.: Influence of time and space correlations on earthquake magnitude. Phys. Rev. Lett. **100**, 038501 (2008)
51. Lippiello, E., Godano, C., de Arcangelis, L.: Dynamical scaling in branching models for seismicity. Phys. Rev. Lett. **98**, 098501 (2007)
52. Lise, S., Paczuski, M.: Self-organized criticality and universality in a nonconservative earthquake model. Phys. Rev. E **63**, 036111 (2001)
53. Middleton, A.A., Tang, C.: Self-organized criticality in nonconserved systems. Phys. Rev. Lett. **74**, 742–745 (1995)
54. Miller, G., Boulter, C.J.: Measurements of criticality in the Olami–Feder–Christensen model. Phys. Rev. E **66**, 016123 (2002)
55. Mori, T., Kawamura, H.: Simulation study of earthquakes based on the two-dimensional Burridge-Knopoff model with long-range interactions. Phys. Rev. E **77**, 051123 (2008)
56. Mousseau, N.: Synchronization by disorder in coupled systems. Phys. Rev. Lett. **77**, 968–971 (1996)
57. Nakanishi, H.: Statistical properties of the cellular-automaton model for earthquakes. Phys. Rev. A **43**, 6613–6621 (1991)
58. Ódor, G.: Universality classes in nonequilibrium lattice systems. Rev. Mod. Phys. **76**, 663–724 (2004)
59. Olami, Z., Feder, H.J.S., Christensen, K.: Self-organized criticality in a continuous, nonconservative cellular automaton modeling earthquakes. Phys. Rev. Lett. **68**, 1244–1247 (1992)
60. Paczuski, M., Maslov, S., Bak, P.: Avalanche dynamics in evolution, growth, and depinning models. Phys. Rev. E **53**, 414–443 (1996)
61. Peixoto, T.P., Davidsen, J.: Network of recurrent events for the Olami–Feder–Christensen model. Phys. Rev. E **77**, 066107 (2008)
62. Pepke, S.L., Carlson, J.M.: Predictability of self-organizing systems. Phys. Rev. E **50**, 236–242 (1994)
63. Pepke, S.L., Carlson, J.M., Shaw, B.E.: Prediction of large events on a dynamical model of a fault. J. Geophys. Res. **99(B4)**, 6769–6788 (1994)
64. Pérez, C.J., Corral, A., Díaz-Guilera, A., Christensen, K., Arenas, A.: On self-organized criticality and synchronization in lattice models of coupled dynamical systems. Int. J. Mod. Phys. B **10**, 1111–1151 (1996)
65. Ramos, O., Altshuler, E., Måløy, K.J.: Quasiperiodic events in an earthquake model. Phys. Rev. Lett. **96**, 098501 (2006)
66. Ramos, O., Altshuler, E., Måløy, K.J.: Avalanche prediction in a self-organized pile of beads. Phys. Rev. Lett. **102**, 078701 (2009)
67. Sammis, C.G., Smith, S.W.: Seismic cycles and the evolution of stress correlation in cellular automaton models of finite fault networks. Pure Appl. Geophys. **155**, 307–334 (1999)
68. Sarlis, N.V., Skordas, E.S., Varotsos, P.A.: Natural time analysis of the Olami–Feder–Christensen model. (to be published) (2011)
69. Sarlis, N.V., Skordas, E.S., Varotsos, P.A.: Nonextensivity and natural time: The case of seismicity. Phys. Rev. E **82**, 021110 (2010)
70. Sarlis, N.V., Varotsos, P.A., Skordas, E.S.: Flux avalanches in $YBa_2Cu_3O_{7-x}$ films and rice piles: Natural time domain analysis. Phys. Rev. B **73**, 054504 (2006)
71. Scholz, C.H.: Earthquakes and friction laws. Nature (London) **391**, 37–42 (1998)
72. Scholz, C.H.: The Mechanics of Earthquakes and Faulting, 2nd ed. Cambridge University Press, Cambridge U.K. (2002)

73. Sicilia, A., Arenzon, J.J., Bray, A.J., Cugliandolo, L.F.: Domain growth morphology in curvature-driven two-dimensional coarsening. Phys. Rev. E **76**, 061116 (2007)
74. Sornette, D.: Critical Phenomena in Natural Science, 2nd edn. Springer, Berlin (2004)
75. de Sousa Vieira, M.: Self-organized criticality in a deterministic mechanical model. Phys. Rev. A **46**, 6288–6293 (1992)
76. de Sousa Vieira, M.: Simple deterministic self-organized critical system. Phys. Rev. E **61**, R6056–R6059 (2000)
77. Su, H., Welch, D.O., Wong-Ng, W.: Strain effects on point defects and chain-oxygen order-disorder transition in 123 cuprate compounds. Phys. Rev. B **70**, 054517 (2004)
78. Varotsos, P., Alexopoulos, K.: Thermodynamics of Point Defects and their Relation with Bulk Properties. North Holland, Amsterdam (1986)
79. Varotsos, P., Ludwig, W., Alexopoulos, K.: Calculation of the formation volume of vacancies in solids. Phys. Rev. B **18**, 2683–2691 (1978)
80. Varotsos, P.A., Sarlis, N.V., Skordas, E.S., Lazaridou, M.S.: Entropy in natural time domain. Phys. Rev. E **70**, 011106 (2004)
81. Varotsos, P.A., Sarlis, N.V., Skordas, E.S., Uyeda, S., Kamogawa, M.: Natural time analysis of critical phenomena. under preparation (2011)
82. Varotsos, P.A., Sarlis, N.V., Skordas, E.S., Uyeda, S., Kamogawa, M.: Natural time analysis of critical phenomena. the case of seismicity. EPL **92**, 29002 (2010)
83. Welling, M.S., Aegerter, C.M., Wijngaarden, R.J.: Self-organized criticality induced by quenched disorder: Experiments on flux avalanches in NbH_x films. Phys. Rev. B **71**, 104515 (2005)
84. Wiesenfeld, K., Theiler, J., McNamara, B.: Self-organized criticality in a deterministic automaton. Phys. Rev. Lett. **65**, 949–952 (1990)
85. Wissel, F., Drossel, B.: Transient and stationary behavior of the Olami–Feder–Christensen model. Phys. Rev. E **74**, 066109 (2006)
86. Yang, X., Du, S., Ma, J.: Do earthquakes exhibit self-organized criticality? Phys. Rev. Lett. **92**, 228501 (2004)
87. Zaitsev, S.I.: Robin Hood as self-organized criticality. Physica A **189**, 411–416 (1992)
88. Zhang, S., Huang, Z., Ding, E.: Predictions of large events on a spring-block model. J. Phys. A: Math. Gen. **29**, 4445–4455 (1996)